

Battery-Free and Wireless Technologies for Cardiovascular Implantable Medical Devices

Jungang Zhang, Rupam Das, Jinwei Zhao, Nosrat Mirzai, John Mercer, and Hadi Heidari*

Cardiovascular disease continues to be one of the dominant causes of global mortality. One effective treatment is to utilize cardiovascular implantable devices (cIMDs) with multi-functional cell sensing and monitoring features that have the potential to manipulate cardiovascular hyperplasia disorders as well as provide therapy. However, batteries with a fixed capacity entail high-risk surgeries for battery-replacement, which causes health hazards and imposes significant costs to patients. This review accesses comprehensive power solutions for cIMDs, from conventional batteries to state-of-the-art energy harvesters and wireless power transfer (WPT) schemes. In particular, WPT has great potential to eliminate the percutaneous wires and overcome frequent battery removal. Here, the fundamentals, power transfer efficiency, antenna design and miniaturization, and operating frequencies in various WPT schemes are presented. Moreover, the power loss attenuation and bio-safety standard (specific absorption rate) for implants are also considered in WPT design envelope. In addition, wireless data transmission of implantable devices from external to internal milieu (and vice versa) along with different modulation and demodulation techniques are investigated. The last advanced power solutions for cIMDs in in-vivo and in vitro research are illustrated throughout. Finally, specifications and future potential of WPT systems in cIMDs are highlighted.

cardiovascular conditions. Typical cardiovascular implantable medical devices (cIMDs), such as pacemakers, defibrillators, ventricular assist devices (VADs), and novel smart stents, are predominately powered by batteries. However, the finite capacity and bulky volume of the battery in the implants hinder long-term use and comfortable deployment. Therefore, these cIMDs require routine surgical interventions to replace the depleted battery, which makes patients prone to suffering from high-risk infections (e.g., bacterial infection) and additional complications (e.g., myocardial rupture). Furthermore, the size reduction of batteries can no longer keep pace with the rapid miniaturization of implantable integrated electronic components. Therefore, novel power strategies are proposed to seek battery substitutes to extend the lifespan of self-powered implants as well as reduce their size.

Recent progress in energy harvesting technology facilitates the investigation of effective battery alternatives. For instance, several energy transducers such as bio-

fuel cells, piezoelectric generators, triboelectric generators, and thermoelectric generators (TEGs) are able to convert in-body energy or external ambient energy^[1] to electricity. In particular, glucose is ubiquitous in the human body, and its energy from the oxidation–reduction reaction can be harvested by enzymatic biofuel cells, which can serve as a power solution for implantable devices. However, the magnitude of power generated by a single biofuel cell is only a few microwatts (μW) based on its in vivo performance, while the power consumption of the cardiovascular implants varies from microwatts to several watts. Therefore, the insufficient power production of biofuel cells impedes its broader applications for cardiovascular implants.

Additionally, the cardiovascular system inherently abounds with redundant energy to provide continuous blood flow through the body, where cardiac output derived from hydraulic power is $\approx 1.4 \text{ W}$.^[2] The advent of piezoelectric and triboelectric energy transducers makes it possible to capture mechanical energy (e.g., heart rate^[3] and aorta pulse^[4]) from the cardiovascular system and directly supply the cardiovascular implants during a long-term operation. Another candidate power source is the thermoelectric generator that can exploit body heat to generate electricity with a power density of up to $35 \mu\text{W cm}^{-2}$.^[5] Such energy harvesting approaches launch a promising prospect

1. Introduction

Advanced microelectronics have increasingly improved the intelligence and miniaturization of cardiovascular devices, which is critical for monitoring, diagnosing, and treating

J. Zhang, R. Das, J. Zhao, H. Heidari
Microelectronics Lab (meLAB)
James Watt School of Engineering
University of Glasgow
Glasgow G12 8QQ, UK
E-mail: Hadi.Heidari@glasgow.ac.uk

N. Mirzai, J. Mercer
College of Medical Science and Veterinary and Life Sciences
University of Glasgow
Glasgow G12 8QQ, UK

 The ORCID identification number(s) for the author(s) of this article can be found under <https://doi.org/10.1002/admt.202101086>.

© 2022 The Authors. Advanced Materials Technologies published by Wiley-VCH GmbH. This is an open access article under the terms of the Creative Commons Attribution License, which permits use, distribution and reproduction in any medium, provided the original work is properly cited.

DOI: 10.1002/admt.202101086

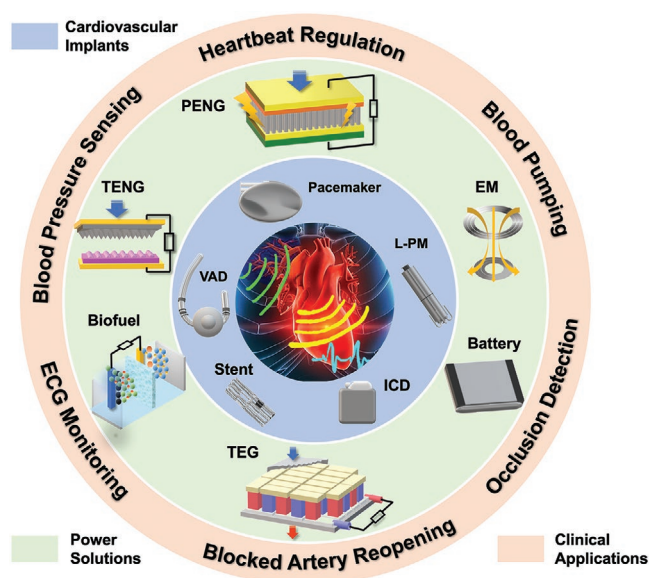


Figure 1. Cardiovascular implantable devices, power strategies, and their medical applications; PENG: piezoelectric nanogenerator, EM: electromagnetic, TEG: thermoelectric generator, TENG: triboelectric nanogenerator, L-PM: leadless pacemaker, ICD: implantable cardioverter defibrillators, VAD: ventricular assist devices.

to replace the battery and charge cardiovascular implants, but they are currently hindered by unstable power generation and percutaneous wires.

The electromagnetic (EM) wireless transfer system has drawn extensive attention for noninvasive powering and monitoring of implantable devices by the electromagnetic energy transfer mechanism. This scheme can simultaneously transmit power and bidirectional data from an adjustable external source to an internal implantable device. Over the last few decades, various wireless power transfer (WPT) links along with their characteristics, such as power transfer efficiency (PTE), transmission distance, and operating frequency have been significantly investigated, from the most established inductive coupling (IC) power transfer and far-field radio frequency (RF) to the emerging magnetic resonant coupling and mid-field WPT. Although WPT is preferable power candidates for the implantable devices, there are still several constraints that require further research and optimization. Particularly, the PTE of inductive coupling WPT is vulnerably affected by the misalignment and transmission distance between the coils, resulting in weak coupling. In addition, the power transfer is suppressed by the body-safety constraints (called specific absorption rate (SAR)) to prevent adverse thermal effects in the tissues. Furthermore, in order to match the ultraminiaturized implants, various antenna types and geometry modifications are investigated to achieve small and efficient antennas. In addition to power strategies for cardiovascular implants, various modulation and demodulation techniques adopted in data transmission system are also explored to detect and control biological parameters in the body.

This paper clarifies power strategies and data transmission schemes of cardiovascular implants, with special emphasis on the wireless power and data transmission system and its future

potential. Section 2 explores the specifications of several cardiovascular implants and their relevant medical applications, which can be observed in **Figure 1**. Moreover, the battery evolution and power requirement in cardiovascular implants are also illustrated in this section. In Section 3, we consider various energy transducers from multiple aspects such as working principles, essential properties, and advanced materials. Finally, the basic principles of wireless power and data transfer system are presented in the Sections 4 and 5, including essential specifications, optimization suggestions, and advanced research in cardiovascular implants. Particularly, the mid-field WPT with patterned metal plates has a great potential to power miniaturized cIMDs in deep tissue among numerous WPT schemes.

2. State-of-the-Art Cardiovascular Implants and Energy Requirements

2.1. cIMDs

It is estimated that 17.9 million people worldwide die from cardiovascular disease every year.^[6] The cardiovascular system consists of a heart and associated blood vessels that convey oxygenated blood and nutrients to perfuse the body with all substrates required for metabolism. The cardiac conduction system of a heart stimulates and coordinates the contractions and relaxations of all four chambers of the heart to transport blood away and around the body and then to the lungs for gas exchange. The coronary arteries and their branches supply the blood to the entire heart muscle but are susceptible to disease such as fibrofatty blockage caused by atherosclerosis. The failures of the cardiac conduction system or vascular can bring occlusion inducement of heart attacks and/or coronary artery disease which can undoubtedly prove fatal. Early intervention in cardiac pathologies offers patients an early-detection and fast-response therapy. cIMDs such as cardiac pacemakers, defibrillators, ventricular assist devices, and novel smart stents have been pervasively regarded as promising treatments which are likely to bring positive and effective solutions to cardiovascular patients.

Figure 2 depicts numerous cIMDs and power schemes along with their development. For instance, the pacemaker was first implanted in 1958,^[7] is the most established cardiac implant and whose technologies continue to improve. Approximately 1.25 million pacemakers are implanted every year, with this number increasing every year.^[8] The pacemaker is specially designed to help detect abnormal heartbeats and adjust them back to normal levels. They can generate the electrical stimulus required to coordinate and restore the heart rhythm by mimicking the sinoatrial node (SAN).^[9] Assisted by several components such as the pulse generator and an array of sensors like accelerometers, piezoelectric crystals and electrocardiogram (ECG) sensors, the pacemaker can detect cardiac-relevant parameters (e.g., minute ventilation, peak endocardial acceleration, and respiratory changes), further regulating the heart rate when its workload exceeds the set threshold.^[10]

Similarly, the implantable cardioverter defibrillators (ICDs) are distinguished by delivering high-level shocks against sudden cardiac death caused by ventricular arrhythmias. VADs are commonly used for end-stage heart failure patients who are

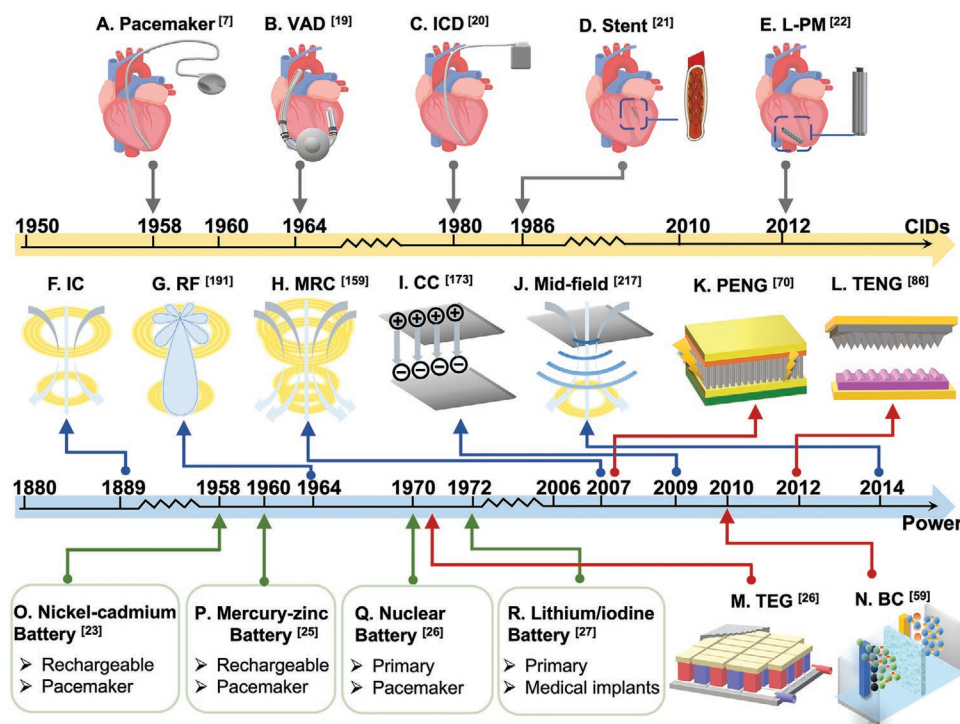


Figure 2. Milestones in the cardiovascular implantable devices and corresponding power strategies: Cardiovascular implants: A) first successful pacemaker implantation in 1958;^[7] B) the first successful implantation of a left ventricular assist device lasted for 10 days until the patient completed the heart transplant;^[19] C) the first ICD was implanted in a patient in 1980;^[20] D) the first coronary stent implanted in a patient coronary artery by Sigwart et al. in 1986;^[21] E) the first leadless pacemaker was implanted in 2012.^[22] Power strategies: F) Nikola Tesla achieved inductive power transfer by using a pair of coils in 1889; G) the first far-field wireless microwave transfer was developed in 1964;^[191] H) magnetic resonant coupling;^[159] I) capacitive coupling;^[173] J) mid-field WPT.^[217] K) The first research work of piezoelectric nanogenerator was developed by Wang and Song in 2006;^[70] L) triboelectric nanogenerator was first invented in 2012 and used to collect mechanical energy in-body and convert it into electrical energy;^[86] M) the nuclear battery is the early form of TENGs;^[26] N) the first biofuel cell implanted in rats in 2010.^[59] O) The first implanted pacemaker was powered by a rechargeable nickel–cadmium battery;^[23] P) battery mercury–zinc battery get involved in powering pacemaker in 1966;^[25] Q) nuclear battery prolonged the lifespan over 15 years and employed in pacemaker from 1970;^[26] R) since 1972, lithium/iodine battery have been the power solution for cardiac implants until today.^[27]

waiting for heart transplantation. VAD is an implantable blood pump that transfers blood from the failure ventricle to the aorta and flows through all the body.^[11] However, conventional VAD runs with a fixed blood flow speed, which cannot adjust the blood flow according to the cardiac demand. Overpumping or underpumping of blood supply can cause pressure imbalance at the interfaces between the device and the heart, and even be fatal. Recently, an adaptive tuning VAD was proposed, which integrated a pressure sensor and a flow sensor to detect and alter blood flow and pressure in real-time.^[12]

Interventional coronary stent placement, called percutaneous (through the skin) coronary intervention (PCI), is a surgical procedure for combatting coronary artery diseases (CADs). CAD frequently occurs on narrow or blocked blood vessels, which is caused by the progressive build-up of plaque, termed atherosclerosis, which can further occlude the blood vessels and reduce oxygen supply to the heart. Current coronary stents are delivered through the femoral or radial arteries and serve as passive mechanical support. By placing the stent on an inflatable balloon, the stent can be directed to the exact point of occlusion. Once the balloon inflated with saline, the stent expands in the artery to reopen the full caliber of the vessel and restore blood flow. However, a postoperative complication

in-stent restenosis (ISR) frequently occurs and is attributable to the formation of thrombosis, the proliferation of smooth muscle cells, and neointimal hyperplasia.^[13] A novel, self-reported stent incorporates a pressure flow sensor and a cell detector to provide a predictive solution to impending vascular complications. More advanced reasons propose protein molecular sensors to detect the smooth muscle cells and clots in the vascular system, with the aim of overcoming in-stent restenosis from early detection^[14] and even deliver appropriate drugs^[15,16] In addition, such smart stents enable continuous monitoring and appropriate treatments like hyperthermia therapy^[17] and drug delivery.^[18]

2.2. Continuous Energy Requirement and Power Management in cIMDs

Successful operation of cardiovascular implants relies on a continuous power supply. Extensive efforts are now being devoted to new power strategies and the development of inexhaustible sources. Figure 2A–N presents the milestones in the evolution of cardiovascular implants and corresponding feasible power strategies over the decades.^[19–22] Emerging cardiovascular

implants with novel power solutions are moving toward smart and fully implanted devices. However, state-of-the-art energy harvesting technologies are still at the level of investigation or animal testing. Batteries remain the dominant power source of cardiovascular implants for clinical and commercial purposes.

Batteries have been used for serving cardiac implants since the first implantable pacemaker, which used a nickel–cadmium battery. This rechargeable battery was depleted after 7 weeks^[23] of implantation and, meanwhile, encountered toxicity and cumbersome charging problems. Subsequently, primary mercury–zinc batteries were employed to powering pacemakers, which can prolong the lifespan of the battery by up to 3 years.^[24,25] In 1970,^[26] the nuclear battery replaced the mercury–zinc battery to support pacemaker deployment. It is an early thermoelectric generator whose electricity is derived from the heat released by decaying radioactive isotopes. Although the lifespan of the mercury–zinc battery is extended to 15 years, this toxic and expensive power source may pose safety hazards due to radiation exposure. The breakthrough of battery application in cardiac implants happened in 1972,^[27] lithium/iodine cells had been successful used in clinical and achieved over 10 years lifespan. Since then, lithium and lithium-ion batteries have become the dominant power strategy to supply implantable devices.

Table 1 summarizes the characteristics of several cIMDs and their power requirements.^[20,28–40] For instance, when defibrillation occurs, the ICD needs to delivery of high voltage electric shocks (provide at least 5 W pulse power for 10 s), so it demands a higher power capability than a pacemaker.^[41] ICDs are frequently powered by lithium/silver vanadium oxide (Li/SVO) batteries, which encounters the problem of delay of shock delivery due to the increasing resistance during discharging.^[42] Recently, other lithium-ion batteries like the lithium manganese dioxide (MDX) battery, the lithium carbon monofluoride have been employed to power the cardiac implants. In particular, silver vanadium oxide ($\text{Ag}_2\text{VO}_2\text{PO}_4$, SVPO) has little effect on the delay of electric shock than the Li/SVO when the resistance increased within the cell.^[43]

Currently, the lithium-ion battery is a pervasive clinical power approach with fixed energy density, limited lifespan, and large size, which is not a permanent and comfortable solution. Repeated battery replacement surgery to vulnerable to high risks patients can induce serious adverse effects. Moreover, the power capability and energy density of the battery are proportional to its volume that cannot satisfy the novel miniaturized implants. Hence, it is imperative to study alternative power solutions for cIMDs.

Table 1. Specifications of cIMDs and their power requirements.

cIMDs	Pacemaker	ICD	VAD	Smart stent
Weight/size	2 g ^{a)} [28] 20–50 g ^{b)} [29]	60 g ^{c)} [30] 130 g ^{d)}	145 g ^{e)} [31] 270 g ^{f)} [32]	8–38 mm ^{g)} , 2.5–4 mm ^{h)} [33]
Lifespan	7.2 years ^[34]	4.9 ± 1.6 years ^[35]	29.7 ± 14.9 days ^[36]	–
Power level	1–10 μW ^[37]	10–100 μW ^[20,38]	5–25 W ^[39]	mW level ^[40]
Power load requirement	High energy density Low rate capability	High energy density High rate capability (30–50 J)	High range of power High rate capability	High energy density Medium rate capability

^{a)}Leadless pacemaker; ^{b)}Transvenous pacemaker; ^{c)}Subcutaneous ICD; ^{d)}Transvenous ICD; ^{e)}50 cc blood displacement volume; ^{f)}90 cc displacement volume; ^{g)}In length; ^{h)}In diameter.

3. Energy Harvesting Strategies in Powering cIMDs

An effective approach to overcome the drawbacks of the battery is to harvest energy from the body so that implantable devices can be self-powered. To drive these devices, abundant chemical, thermal, and mechanical energy from the human body can be harnessed as sustainable renewable energy sources extracted via various energy transducers. In particular, four types of energy transducer: biofuel cells, piezoelectric generators, triboelectric generators, and thermoelectric generators are attractive for powering implantable devices, as presented in **Figure 3A–D**. In order to determine the power feasibility of in-body energy in the field of cardiovascular implantable devices supply, the aforementioned energy transducers have been investigated in this paper based on their fundamentals, power generation, and in vivo animal experiments.

3.1. Biofuel Cell

Biofuel cells have received considerable attention since their significant progress in in vivo animal tests. The concept of biofuel cells was developed in the early 1960s^[44] until the breakthrough of biofuel cells made in the 20th century provided an encouraging alternative power solution for implantable devices. The working principle of the biofuel cells is the same as that of electrochemical batteries based on redox reactions. Biofuel cells employ renewable enzymes or microbes as the catalyst rather than using metals as catalyst in electrochemical batteries. Moreover, biofuel cells extract chemical energy from continuous biofuel in blood flow (e.g., glucose, lactose) that can be replenished, while electrochemical batteries are limited by fixed fuel, and need to be replaced when it is depleted.

Biofuel cells can be classified into microbial fuel cells and enzymatic fuel cells (EFCs) according to the biocatalyst type. Microbial fuel cells exploit living microorganisms (e.g., bacteria) as the biocatalyst, where the power generation is significantly influenced by the microbial metabolism^[45] and culture condition (e.g., temperature and potential of hydrogen (PH)^[46,47]). Although microbial fuel cells offer a durable operating period (more than 5 years) due to the long lifespan of living microorganisms,^[48] this type of cell exhibits low power density owing to the resistance of cell membranes and low catalytic activity.^[49] In contrast, enzyme-based fuel cells have been

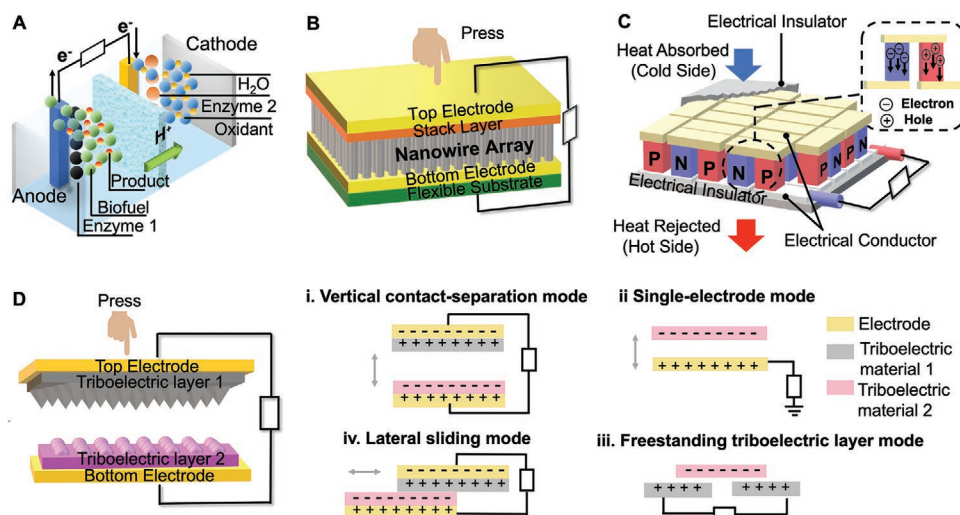


Figure 3. Energy harvesters: A) biofuel cell, B) PENG, C) thermoelectric generator, and D-i-iv) TENG and four working modes of TENGs.

extensively studied for energy conversion due to their higher power density (expressed in mW cm^{-2})^[50] than microbial fuel cells. However, enzymes are easy to be degraded, resulting in an enzyme fuel cell's lifespan usually of 7–10 days.^[48]

A typical enzymatic biofuel cell consists of an anode and cathode, which are separated by a proton exchange membrane, as shown in Figure 3A. At the anode, the enzyme catalyzes the oxidation reaction of a biofuel while releasing electrons to reach the electrode surface and then traveling to the cathode via external wires. Meanwhile, protons produced by the anode migrate to the cathode and complete the reduction reaction with an oxidant and electrons. The performance of enzyme fuel cells is mainly determined by electron transfer between the enzyme and electrode.^[51] Two major transfer mechanisms are adopted to establish effective electrical communication in enzyme fuel cells: mediated electron transfer (MET) and direct electron transfer (DET).^[52] DET carries out the electrons from the active site of the enzyme directly to the electrode surface, while MET requires a mediated molecule (mediator) as an electron transfer relay to shuttle the electrons to the electrode. In general, redox-active modules and polymers act as electron donors and acceptors between the enzyme and electrode surface, making the redox potential close to the active center of the enzyme.^[53] In addition, MET has a faster electron transfer speed than DET due to its shorter electron mobile distance (within 2 nm). However, the MET-based biofuel cells may cause safety issues and low open-circuit voltages induced by the potential difference between the active site of the enzyme and the mediator.^[54] Therefore, the DET method is widely employed in biofuel cells due to its simple structure.

The significant breakthrough in biofuel cells in animal implementation offers a potential solution for cardiovascular implants. A glucose enzyme-based biofuel cell was implanted in a lobster and generated an open-circuit voltage (V_{oc}) of 0.54 V.^[55] To enhance the V_{oc} , they found that two series-connection biofuels in two separate lobsters doubled the V_{oc} up to 1.2 V. Moreover, they designed a biofuel cell array that consists of 5 individual biofuel cells connected in series in human

serum solutions filled with concentration of glucose (for mimicking the human blood circulatory system) to power the pacemaker. As expected, a 2.8 V of V_{oc} was obtained, and the pacemaker worked as normal after being connected with the biofuel cell array. Another study employed carbon nanotubes (CNTs) as electrodes of the biofuel cell and implanted in a snail. In particular, the researchers adopted the DET mechanism in the biofuel cell, which is conducive to the effective immobilization of enzymes on electrodes, resulting in a power of $7.45 \mu\text{W}$ and a V_{oc} of 0.53 V.^[56] Subsequently, the same team^[57] developed a comparative study in which implanted three biofuel cells in three independent clams, connecting in series and parallel, respectively. Three series array biofuel cells delivered peak power of $5.2 \mu\text{W}$ with a V_{oc} of 0.8 V, while the parallel one obtained a 0.36 V of V_{oc} and $37 \mu\text{W}$ of maximum power, respectively. However, the feasibility of biofuel cells for powering biomedical implants cannot be fully demonstrated by aforementioned experiment in invertebrates. Therefore, a biofuel cell was implanted in a mammal (in a rat cremaster tissue) to harvest the electricity.^[58] The CNTs were applied at enzyme-modified electrodes and obtained a stable V_{oc} of $140 \pm 30 \text{ mV}$ and a $0.35 \mu\text{W}$ of maximum power. Another biofuel cell^[59] was also implanted in a rat but placed in retroperitoneal space, in which both electrodes were based on the compacted graphite disc (containing ubiquinone and glucose oxidase at the anode, while polyphenol oxidase and quinone at the cathode). The biofuel cell was measured in vivo with a power production of $6.5 \mu\text{W}$ under 0.13 V and then dropped to a stable power of $2 \mu\text{W}$ after several hours. Later on, a study on biofuel cells was carried out in the blood vessel of a rabbit ear.^[60] In particular, to prevent the blood clot from covering the electrode surface, they coated 2-methacryloyloxyethyl phosphorylcholine (MPC) polymer on electrodes to achieve biocompatibility in vivo and generated power of $0.42 \mu\text{W}$ at 0.56 V, while the control group without the MPC coating presented a 40% reduction of output power. To verify the sustainability of biofuel cells for operating biomedical implants in vivo, El Ichi-Ribault et al.^[61] implemented a wireless tele-transmission system in a rabbit to

monitor the variation in the biofuel cell for two months. During the first week of implantation, the V_{oc} remained at a range of 0.65–0.68 V and then obtained a stable V_{oc} of 0.42 V after 18 days. Moreover, the inflammatory action and biofouling caused a sharp drop in voltage of implanted biofuel cell in the first week and subsequently became steady.

While several biofuel cells have been explored in vivo experiments in animals, the output level (sub μ W, $V_{oc} < 1$ V) produced by biofuel cells can not satisfy the power consumption of cIMDs except for the ultralow-power pacemakers. Moreover, there remain hurdles in the practical deployment of enzyme biofuel cells. In particular, the efficient electron transfer between the enzyme active site–electrode interface and the enzyme immobilization are the primary issues for improving the overall power generation. To this end, the nanostructured conducting CNTs have been developed to facilitate the electron transfer rate, stability, and concentrations of enzymes. CNTs possess superior biocompatibility and large electroactive surface (1–10 nm²) which benefits the enzyme–electrode interface. Furthermore, the operation period and the inflammatory response of biofuel cells in vivo impede their application in implantable devices.

3.2. Piezoelectric Transducer

Piezoelectric transducer is a prominent candidate for converting scavenging vibrational energy into electricity to drive implantable devices. Piezoelectric transducers are characterized by higher energy density (35.4 mJ cm⁻³) compared to electrostatic (4 mJ cm⁻³) and electromagnetic (24.8 mJ cm⁻³) transducers.^[63] The piezoelectric transducers benefit from their smart piezoelectric materials with inherent transduction capacity, while the other transducers require additional conditions to generate electricity, such as external source (electrostatic transducers), induction magnetic field (electromagnetic harvesters), and frictional contact (triboelectric generators).^[64] Furthermore, piezoelectric materials can generate the opposite electric charges in response to the mechanical strain, known as the piezoelectric effect. In the exploration of vibration energy, piezoelectric transducers have drawn considerable attention in academia. In particular, the cardiovascular system can supply mechanical energy to cardiovascular implants from heart contraction/relaxation, blood circulation, and arterial pulsation. However, piezoelectric generators require sensitive transducer structures and stretchable piezoelectric materials due to slight vibrations of heart motion (vibrational frequency of 1–1.34 Hz^[65]) and the vulnerability of the heart.

3.2.1. Piezoelectric Materials

Piezoelectric materials have been extensively explored to generate power from kinetic since the piezoelectric effect was first discovered by Pierre and Jacques Curie in 1880,^[66] which has a significant impact on the performance and applications of piezoelectric transducers.

Ceramic materials such as lead zirconium titanate (PZT) and barium titanate (BaTiO₃) are the most broadly used

piezoelectric materials in piezoelectric transducers, which possess high dielectric constant (PZT: 200–5000, BaTiO₃: 1700) and superior piezoelectric coefficient (PZT: $d_{33} = 100$ –1000 pC N⁻¹, BaTiO₃: $d_{33} = 190$ pC N⁻¹).^[67,68] However, the brittleness and toxicity properties of PZT are unacceptable for implantable devices. On the contrary, polymeric materials are characterized by superior flexibility and biocompatibility, but suffering from low sensitivity and efficiency. In particular, the typical polymer material polyvinylidene fluoride (PVDF) possesses a 30 pC N⁻¹ piezoelectric coefficient (d_{33}),^[69] which is ten times lower than that of ceramics. In order to realize high flexibility and piezoelectricity on piezoelectric materials, various types of composites and nanomaterials have been investigated. In 2006, Wang and Song^[70] initially proposed a piezoelectric nanogenerator (PENG) based on zinc oxide (ZnO) nanowires. When the ZnO nanowire is deformed by an atomic force microscope (AFM) tip, it will generate a strain field and the charge separation, as illustrated in Figure 3B. In addition, novel composite piezoelectric materials (mix polymeric piezoelectric materials with inorganic materials) can overcome the shortcomings of ceramic materials and polymeric materials have also attracted great attention. For instance, Lu et al. prepared a PZT in form of layer stacks and printed it onto a flexible polyimide substrate (Kapton), packaging with polydimethylsiloxane (PDMS) encapsulation.^[71] This ultraflexible piezoelectric transducer extracted the cardiac motion of a swine and generated a 3 V peak-to-peak voltage. Alternatively, another type of composite uses flexible polymers filled with biocompatible ZnO nanoparticles. For instance, by adding ZnO nanoparticles and multiwall carbon nanotubes (MWCNTs) in PDMS-infilled PVDF-TrFE composite film, Xu et al.^[72] developed a nanomaterial-mediated polyvinylidene fluoride-trifluoroethylene (PVDF-TrFE) film. This promising film combines the merits of ZnO nanoparticles and PDMS, enhancing the piezoelectricity and sensitivity, respectively. Moreover, they designed a multibeam PEG to support a pacemaker based on this film and generated an output of 3.22 ± 0.24 V. Recently, Azimi et al.^[73] proposed a composite PVDF nanofiber containing hybrid nanofillers of ZnO and reduced graphene oxide (rGO). In order to evaluate the feasibility of the polymer composite-based PENG in powering pacemakers, an in vivo implantation has been carried out in a dog and yielded 0.487 μ J per heartbeat. In addition, the recent emergence of single crystals is regarded as an alternative piezoelectric material of PZT ceramics due to their exceptional piezoelectric performance. For instance, the piezoelectric coefficient ($d_{33} > 2000$ pC N⁻¹) and electromechanical coupling coefficient ($k_{33} > 0.9$) of lead magnesium niobate-lead titanate (PMN-PT) exhibits are several times higher than that of PZT.^[74] In a paper by Hwang et al.,^[75] a self-powered cardiac pacemaker in a living rat was powered by a PMN-PN energy transducer. This PENG used the PMN-PT single crystal on a polyethylene terephthalate (PET) substrate, and successfully collected an open-circuit voltage of 8.2 V and a short-circuit current of 0.223 mA.

3.2.2. Piezoelectric Transducer Structure

Cantilever beam piezoelectric transducers are the most established and extensively used transducers for vibration harvesting.

Table 2. Cantilever-type piezoelectric transducers and PENGs in the applications of powering cIMDs.

Energy source and refs.	cIMDs	Piezoelectric materials	Transducer type	Max output (power/energy/ V_{oc}/I_{sc}) (power density)	DimensionVolumeThickness
Heartbeat 2012 ^[77]	Pacemaker	PZT-5A ceramics	Cantilever-type (zigzag)	$1.3 \times 10^{-2} \mu\text{W mm}^{-2a)}$	$27 \times 27 \times 6 \text{ mm}^3$
Heartbeat 2014 ^[75]	Pacemaker (trigger energy of 1.1 μJ)	PMN-PT single crystal	Thin film	8.2 V, 145 $\mu\text{A}^a)$ 2.7 $\mu\text{J}^{b),c)}$	1.7 cm \times 1.7 cm
Heartbeat 2015 ^[71]	Pacemaker	PZT ceramics	Nanogenerator	3 V ^{d)}	400–600 nm (thickness)
Heartbeat 2017 ^[78]	Pacemaker	PZT ceramics	Cantilever-type (fan-folded)	16.25 $\mu\text{W}^a)$	1 cm^3
Heartbeat 2019 ^[3]	Pacemaker	Piezoelectric composites	Multiple layers structure	36 V, 22 μA , 33 $\mu\text{W}^{a),e)}$ 20 V, 8 $\mu\text{A}^{b),e),f)}$ 22 V, 40 μA , 14 $\mu\text{W}^{a),g)}$ 12 V, 15 $\mu\text{A}^{b),f),e)}$	100 μm (thickness)
Heartbeat 2020 ^[72]	Pacemaker	PDMS-infilled microporous P(VDF-TrFE)	Cantilever-type (multibeam)	$3.22 \pm 0.24 \text{ V}^a)$	6 mm (thickness)
Heartbeat 2021 ^[73]	Pacemaker	Nanofibers of PVDF and hybrid nanofillers	Nanogenerator	$24.52 \pm 1.11 \text{ V}$ $19.39 \pm 1.08 \mu\text{A}^a)$ 0.487 μJ per heartbeat ^{b),h)}	1.5 cm \times 1.5 cm
Ascending aorta pulse 2015 ^[4]	Pacemaker/ICD/cardiac monitor	PVDF and Al layer	Thin film	10.3 V, 400 nA, 681 nW ^{a)} 1.5 V, 300 nA, 20 nW ^{b),i)}	56 mm \times 56 mm 200 μm

^{a)}In vitro; ^{b)}In vivo; ^{c)}In the cardiac muscle of the rat; ^{d)}In the cardiac of the swine; ^{e)}Two piezoelectric composites connected in series mode; ^{f)}In the heart of the porcine; ^{g)}Two piezoelectric composites connected in parallel mode; ^{h)}In the heart of the dog; ⁱ⁾In the ascending aorta of the porcine.

Since its higher strain generation for a given force input compares with other types of piezoelectric transducers (e.g., circular diaphragm, cymbal type, and stack type),^[76] This simple type of transducer can generate significant power under excitation of vibration frequencies in the body. However, extra-low vibration frequencies from cardiovascular systems hinders the amount power generation of piezoelectric transducers. To overcome the resonance matching and miniaturization problems of piezoelectric transducers, plenty of studies on the configuration of cantilever beams have been carried out. Compared with conventional cantilever beams, Amin Karami and Inman^[77] initially proposed and proved that flat zigzag-shaped transducers can significantly increase the power density and reduce the natural frequency of piezoelectric transducers. This solution was achieved by reducing the stiffness of beams and eliminating torsional effects in the structural design of multiple cantilever beams, generating 10 μW power under the excitation of heartbeats. Since then, the advent of other cantilever shapes (including fan-fold shape^[78] and elephant shape^[79]) have improved the performance of piezoelectric transducers at low vibrational frequencies.

Recently, advanced PENGs with nanostructures exhibit superior flexibility and stretchability under an off-resonance mechanism. A PENG consist of a pair of top and bottom electrodes in a sandwich structure.^[80] When the nanowires are bent by an AFM tip, PENG generates electric charge polarization and induces an electric field, thereby forming a Schottky barrier between nanowires and metal contacts.^[70] Therefore, PENGs can provide great potential in improving energy conversion efficiency and arouse significant interest in self-powered micro/nanoscale implantable devices

Table 2 summarizes several bulk cantilever-type piezoelectric transducers and PENGs in applications of using cardiovascular vibrations to power cIMDs, as well as their design parameters and output performance. In addition, piezoelectric transducers need to be attached to the heart to harvest heartbeats vibration, but the movement of heart is complicated and random. The placement of piezoelectric transducers on the heart affects their output performance. Particularly, Lu et al.^[71] implanted a PENG in a swine and verified that the output signal is strongly related to the location and orientation of the PENG placement. They found that the optimal position is between the left apex of the ventricle and the right ventricle of the heart, where the maximum power can be output. Moreover, Li et al.^[3] compared 4 sites on the pig's heart and identified the maximum output is at the apex of the heart.

3.3. Triboelectric Nanogenerator (TENG)

The kinetic-electricity conversion can also be realized by TENGs, which generate electricity based on the coupled triboelectrification and electrostatic induction.^[81] Since almost every material has a triboelectrification effect at different levels (referring to triboelectric series table^[82]), TENGs have a wider range of materials to select from than PENGs. However, the TENG requires two contacting or sliding materials to create the triboelectric charge by rubbing between their surfaces, while PENGs simply generate charges through deformation of piezoelectric materials. TENGs work upon the principle of triboelectric effects, in which certain materials are in frictional contact and then separated from each other, driving electrons to transfer between different materials, and further generating current.^[83] On the basis of this

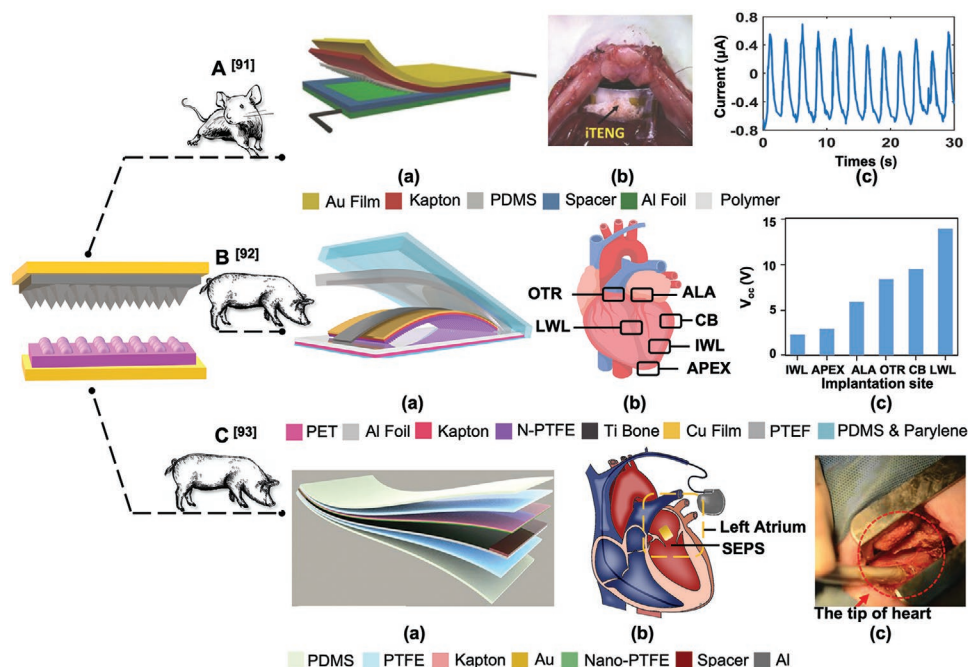


Figure 4. TENG applications in powering cardiovascular implants in vivo: A) the implanted TENG harvested the periodic breathing in a living rat to drive the pacemaker. a) The structure of the fabricated TENG, b) the TENG implanted in a live rat, and c) The current output of the implantable TENG. B) The implanted TENG was driven by the heartbeat of a porcine for achieving a self-powered wireless cardiac monitoring system. a) Schematic structure of the TENG, b) different implant sites on the cardiac: OTR, the right ventricular; ALA, the right ventricular; ALA, the auricle of the left atrium; CB, the cardiac base; LWL, the lateral wall of the left ventricular; IWL, the inferior wall of the left ventricular; and c) the output V_{oc} at different implant sites. C) The TENG collected the energy from blood flow to support the endocardial pressure sensor in a porcine model. a) Schematic structure of the TENG, b) the implant site in the swine's heart, and c) the figure of in vivo experiment. A–a,b) Reproduced with permission.^[91] Copyright 2014, Wiley-VCH. B–a) Reproduced with permission.^[92] Copyright 2016, American Chemical Society. C–a,c) Reproduced with permission.^[93] Copyright 2019, Wiley-VCH.

principle, four fundamental working modes of TENGs: vertical contact-separation mode, lateral sliding mode, single-electrode mode, and freestanding triboelectric layer mode^[84] have been developed for different target applications, which are presented in detail in Figure 3D–i–iv and paper.^[85]

The first TENG was proposed by Wang and co-workers^[86] in 2012 as an effective energy harvesting technology. It possesses numerous merits including broad material availability, lightweight, and flexibility, which makes TENG considered an ideal power solution in the applications of low-consumption implantable devices.

Currently, the main challenge is to generate high output through effective TENGs. In this regard, triboelectric material pairs matching with strong electron affinity has a significant impact on the output of TENGs. In general, certain triboelectric materials (tendency to gain electrons) such as polytetrafluoroethylene (PTFE), PDMS, Kapton, terephthalate (PET), and Fluorinated ethylene propylene (FEP) are commonly coupled with other specific materials (tendency to lose electrons) such as aluminum (Al), gold (Au), copper (Cu), and silver (Ag).

In addition, the surface charge density on the triboelectric layers also determines the electric output of TENGs. In order to further improve the output performance, numerous studies have explored surface-modified TENGs, which can be divided into four categories: physical, chemical, biological, and hybrid modification.^[87] Among them, physical modification (controlling surface morphology and interlayer interaction) and

chemical modification (adjusting the surface-charging tendency and modifying the interfacial potential) are widely employed to increase the electric output of TENGs.^[88] In particular, the physical surface nanostructure modification is the most common and efficient way. This method introduces diverse nanostructures with the aim of enhancing the surface roughness and effective contact area, thereby increasing the charge density between the triboelectric layers.^[89] Paper^[88,90] reviewed exhaustive surface engineering techniques and novel modified materials in TENGs, we will not elaborate them here.

Since Zheng et al.^[91] realized the first implantable TENG, flexible and lightweight TENGs have been significantly encouraging in powering cardiovascular devices. They utilized the TENG to harvest the periodic breathing of a rat and successfully drive a pacemaker, as shown in Figure 4A. A PDMS film with patterned pyramid arrays and nanosurface modified Al foils are employed as a pair of triboelectric layers, in which Au and Al film are served as electrodes. The introduced flexible PDMS and Kapton layers exhibit high flexibility and biosafety. The TENG tested 12 V of V_{oc} and 0.25 μA of I_{sc} output in vitro and harvested 3.73 V of V_{oc} and 0.14 μA of I_{sc} in vivo, respectively. Subsequently, this team proposed a new TENG that was continuously powering the cardiac monitoring system in a porcine in vivo over 72 h,^[92] as illustrated in Figure 4B. Notably, the friction layers and electrodes materials are the same as before, but a highly resilient titanium strip was added to the TENG structure to ensure effective contact

and separation in vivo. After being encapsulated by PDMS and parylene C, the TENG measured 45 V of V_{oc} and a 75 μA of I_{sc} in vitro and collected 14 V V_{oc} and 5 μA I_{sc} from contraction/relaxation movement of the heart in vivo. In addition, tests were located differently on the heart to validate the placement with optimal output performance. Consequently, they found that place the TENG on the lateral wall of the left ventricular can produce the best output. As depicted in Figure 4C, Liu et al.^[93] devoted to monitoring severe heart failure through a self-powered endocardial pressure sensor, which was inserted into the left ventricle of a porcine. This research demonstrates that TENGs can collect mechanical energy from the blood flow in the heart chamber to power the endocardial pressure sensor. They used a corona discharge method to modify the surface of the nano-PTFE film (acting as one triboelectric layer) to increase the surface charge density, and the Al foil was employed as the other triboelectric layer. Furthermore, Au layer and Al foil were acted as a pair of back electrodes, and a 3D ethylene-vinyl acetate (EVA) copolymer film was used as a spacer between them. The result shows that the output voltage enhanced from 1.2 to 6.2 V after the surface modification. In 2019, Ouyang et al.^[94] demonstrated a symbiotic pacemaker powered by a multilayer-structure TENG. In order to improve the output performance, this study adopted several methods including: employing a nanostructured PTFE triboelectric layer, adding a spacer layer to increase the effective contact area, and introducing the corona charge method to improve surface charge density. In addition, this TENG was fully packaged with flexible Teflon and PDMS films to achieve leak-free structure and stretchability. As a result, the TENG was mounted between the heart and pericardium of a porcine, generating 0.495 μJ energy during each cardiac motion cycle. In summary, various explorations of TENGs, including advanced materials, effective multilayer structures, and placements in vivo have greatly promoted their output performance and applications in cardiovascular implants.

3.4. Thermoelectric Generator

Human body waste heat can be directly converted into electricity through TEGs, which also launch a substitute for powering biomedical implants. In the battery section of this review, the TEG has been mentioned as an early transducer for powering the pacemaker by extracting heat from the radioactive isotope decay of nuclear batteries. With the remarkable development of microscale and nanoscale generators, the emerging TEGs can harvest energy from temperature gradients in human tissue based on the Seebeck effect.^[95] The basic module of TEGs is a thermocouple, which consists of a pair of n-type and p-type semiconductor legs connected to electrodes, as shown in Figure 3C. TEGs arrange multiple thermocouples electrically in series and thermally in parallel in a sandwich structure of two insulator layers (or ceramic substrate). Besides, doped semiconductors contain a large number of free carriers, which are holes in p-type materials and electrons in n-type materials.^[96] When a thermocouple is subjected to a temperature difference, the Seebeck effect occurs, which allows carriers to migrate from the hot side to the cold side, thereby

generating a voltage. The output voltage produced by a TEG is proportional to the temperature gradient, and the formula is shown as follow^[96]

$$V_{out} = n \cdot \Delta T (\alpha_1 - \alpha_2) \quad (1)$$

where n is the number of thermocouples, ΔT is the temperature difference across the TEG, and α_1 , α_2 are the Seebeck coefficients.

The power transfer efficiency of a TEG is determined by the temperature difference, thermoelectric material features, where the equation can be expressed as Equation (2)^[97]

$$\eta = \frac{\Delta T}{T_h} \frac{\sqrt{1+ZT} - 1}{\sqrt{1+ZT} + T_c/T_h} \quad (2)$$

where T is the average temperature, and T_h and T_c are the temperatures of the hot plate and the cold plate, respectively. The figure of merit (ZT) is a significant factor to evaluate the performance of thermoelectric materials, which can be defined as follow^[98]

$$ZT = \frac{S^2 \sigma}{k} T \quad (3)$$

where S is the Seebeck conductivity, σ is the electrical conductivity, and k is the thermal conductivity.

Since semiconductors materials (such as bismuth telluride (Bi_2Te_3), antimony telluride (Sb_2Te_3), and lead telluride ($PbTe$) alloys) possess a high value of ZT ($ZT > 2$ ^[99]), these materials have been widely employed. However, these inorganic materials have some disadvantages, such as toxicity and rigidity, which are inappropriate for implantable devices. Therefore, conductive polymer materials such as polyaniline (PANI), polyimide (PI), and poly(3,4-ethylenedioxythiophene)-poly(styrenesulfonate) (PEDOT:PSS) are attractive due to the flexibility, biocompatibility, and inherent low thermal conductivity. Nevertheless, these organic materials have a low value of ZT (between 0.01 and 0.25^[100]), which is 2–3 orders lower than that of semiconductor materials.^[101] Therefore, organic–inorganic hybrid materials combine the merits of the two and show bright prospects in thermoelectric materials. Effective methods to develop flexible and high thermoelectric performance materials include nanostructure engineering technology and the semiconductor doping methods (e.g., PANI/graphene thermoelectric composite films,^[102] and tellurium–PEDOT:PSS hybrid composites^[103]). Additionally, the innovation in hybrid materials and more detailed features are reported in papers^[101,104]

In addition to the investigation of materials, temperature difference is another decisive factor for improving efficiency (as presented in Equations (2) and (3)). Several academics have studied the maximum heat gradient across the body and found that the largest difference (ΔT) occurs in the fat layer (near the skin layer)^[105,106]

A TEG made of doped bismuth telluride materials was reported by Bhatia et al.,^[107] which employed nearly 4000 thermocouples in series to charge pacemakers and/or defibrillators. The surface area of the TEG is 6 cm^2 and requires a 2 $^\circ C$ of ΔT to drive. This is easy to fulfil due to the 5 $^\circ C$ temperature

difference in multiple parts of the body. The TEG generates 4 V of V_{oc} and 100 μW of output power, which presents great potential for powering low-consumption cardiac implants. In addition, Yang et al.^[108] presented a prototype of TEG equipped with a specific boost circuit for powering a pacemaker. Moreover, they verified the energy harvesting circuit by utilizing a higher power consumption clock circuit (145 μW) instead of a real pacemaker (with the same pulse interval). When the temperature gradient stabilized at 0.5 °C in a rabbit, the output voltage was measured as 20 mV and then rose to 3.3 V after passing through the boost circuit.

Although previous studies have demonstrated the feasibility of converting body heat into useable electricity that can be used to power cardiac implantable devices, there are few reports in the field of implantable TEGs according to the latest research on energy transducers area. In general, the development of TEG in biomedical applications is hindered by the following basic limitations:

- A) The design and layout of thermoelectric transducers with hundreds or even thousands of thermocouples are hindered by the ultrasmall surface area.
- B) The amount of power generation is limited by temperature gradient in body.
- C) The time-variant temperature difference needs to be maintained all the time.

4. Wireless Power Transfer Solutions in cIMDs

The rapid growth of research in energy harvesting technology has led to significant improvements in power solutions for low-consumption cardiovascular implants such as pacemakers and defibrillators. However, the in vivo output collected from energy harvesters is too insufficient to be utilized as an alternative power solution for other higher power level cardiovascular implants. Electromagnetic wireless power transfer is an actively adjustable power strategy that can regulate the input voltage to provide stable and adequate support for the load. This is a promising power solution that uses EM energy between the internal receiver and external transmitter to support various wearable and implantable devices without percutaneous wires and batteries (e.g., contact lens,^[109] brain,^[110] neural,^[111] and cardiovascular medical devices).

When the wireless implants are initially implanted in the patients, the cIMDs should be disconnected from the external controller.^[112] The external programmer will send a modulated wake-up signal to the implantable receiver through a wireless link. The receiver detects the signal and then activates the rest of the chip. In detail, a low dropout (LDO) regulator is needed to generate a stable voltage to support implantable devices. The voltage regulator output is disconnected from the implanted capacitor during startup, which is controlled by a power-on reset (POR) circuit. When the power supply voltage reaches the POR activation threshold, the POR circuit sends out a power-on signal to initialize the chip and start working.^[113] It is expected that WPT technology will lead to fully self-reported implantable devices in the future. To evaluate and optimize the performance

of WPT in powering cardiovascular implants, this review investigates three significant aspects:

- A) Miniaturization and compactness of advanced antennas for cardiovascular implants and their radiation performance.
- B) Human body safety guidelines when exposed to electromagnetic fields and the investigation of changes in dielectric properties under different frequencies.
- C) The basic principles and power transmission efficiency of various WPT links.

In this section, the specific characteristics and potentialities of different WPT schemes and their state-of-the-art applications in cardiovascular implants are discussed.

4.1. Antenna Design and Miniaturization of cIMDs

An antenna is one of the most vital components in WPT, used to transmit and receive signals. In particular, the antenna design is the basic and indispensable work to guarantee efficient power transmission. Herein, we review the types, geometries, and performance of miniaturized and compact antennas used in cIMDs. Advanced WPT technology for powering implantable devices requires simultaneous miniaturization and high-performance implantable antennas. Planar antennas,^[114] in particular the rectangular microstrip antenna^[115] circular patch antenna,^[116,117] PIFA antenna^[118] are preferred for small size antenna. These antennas benefit from their simple design and fabrication, are also easily integrated with other electronic components.

In order to further meet the requirement of ultrasmall implantable antennas, the antenna size can be reduced by following methods:

- A) Geometry configuration: Folded configuration can shrink the size of antenna by increasing the current flowing path, such as meander-shape,^[119] spiral-shape,^[120,121] and fractal structure.^[122] The effective dimensions of an antenna will increase in the form of the meander and/or spiral configuration, which allows increasing the physical path for surface current flow, and ultimately leads to the decrease of resonant frequency compared to the conventional antenna.^[123] Moreover, the antenna size reduction factor β depends critically on the number of meander elements per wavelength and the width of the rectangular loops, which is defined as in Equation (4)^[124,125]

$$\beta = l/L \quad (4)$$

where L is the length of the conventional monopole and l is the length of the meander antenna with the same resonant frequency.

- B) High dielectric substrate materials: As previously mentioned, the propagation of EM waves is affected by dielectric properties and frequencies. Therefore, the introduction of a high dielectric constant is capable of decreasing

Table 3. Antenna types and geometry modifications applied in cardiac implants.

Antenna type	Geometry modification	Operating frequency	Dimension [mm ³]	Antenna parameters			SAR [W kg ⁻¹]	Bandwidth	S ₁₁ [dB]	Gain [dBi]	Test scenarios
				Substrate	Superstrate	Feed					
Microstrip antenna ^[130]	Meander-shaped	2.46 GHz ^{a)}	40 × 30 × 3.3	Rogers R03010 (ε _r = 10.2)	Rogers R03010	Waveguide	–	1.637 GHz	–28.37	–	2/3 muscle equivalent phantom (ε _r = 38.1, σ = 0.53 S m ⁻¹)
Microstrip patch ^[131]	Meander-line	2.4 GHz ^{b)}	3 × 4 × 0.5	Rogers RT/duroid6010 (ε _r = 10.2)	Rogers RT/duroid6010	Coaxial probe	31.04 ^{d)} 270.28 ^{d)}	21.88%	–19	–25.95	Heart phantom box and minced pork muscle
Microstrip patch ^[120]	Spiral-shaped	403 MHz ^{e)}	11.9 × 18.2 × 3.8	Rogers RT/duroid6010	Rogers RT/duroid6010	Coaxial probe	2.74 ^{d)}	–	–17.5	–	2/3 human muscle box (σ = 0.6463 S m ⁻¹ , ε _r = 42.807)
Microstrip patch ^[132]	Spiral-shaped ^{f)}	402 MHz ^{e)} 2.45 GHz ^{g)} 1.6 GHz ^{h)}	17.15 × 6.5 × 0.377	Rogers RT/duroid 6010	Rogers RT/duroid 6010	Coaxial probe	588 ^{d)} 441 ^{d)} 305 ^{d)}	148 MHz 219 MHz 171 MHz	–36 –24 –20	–30.5 –18.2 –22.6	Homogeneous body model
Circular patch ^[133]	Spiral-shaped	403 MHz ^{e)}	Radius = 5 mm, thickness = 0.89 mm	Rogers RO 3006 (ε _r = 10.2)	Rogers RO 3210 (ε _r = 6.4)	Coaxial probe	–	–	–20	–	Homogeneous and inhomogeneous heart muscle
Microstrip patch ^[134]	Cut off two diagonals	2.45 GHz ISM band	40 × 40 × 0.635	Rogers RO 6010	–	Coaxial probe	40.6 ^{d)}	37.74%	–12	–15.87	Three-layered chest model and minced pork

^{a)}ISM band (2.4–2.48 GHz); ^{b)}ISM band; ^{c)}SAR_{10g}; ^{d)}SAR_{1g}; ^{e)}MICS band (402–405 MHz); ^{f)}With an open-end slot in the ground; ^{g)}ISM band (433.1–434.8 MHz and 2.4–2.48 GHz); ^{h)}Mid-field band (1520–1693 MHz).

the guided wavelength and the length of a patch, which gives the following equation^[126]

$$L = \frac{\lambda_g}{2} = \frac{C}{2f\sqrt{\epsilon_{\text{eff}}}} \quad (5)$$

where L is the length of the patch antenna, λ_g is the guided wavelength, C is the speed of light, and ϵ_{eff} is the effective dielectric constant. However, the drawback of this approach is that it narrows the bandwidth of the antenna and losses surface-wave.^[127]

- C) Superstrates: The introduction of a superstrate on a microstrip antenna is beneficial to simultaneously reduce the size and enhance the gain and bandwidth of the antenna by forming a larger in-phase electric field on the superstrate surface.^[128]
- D) Shorting pins: By deploying shorting pins connecting the patch and the ground plane of the microstrip patch antennas can be utilized for compressing the size of antennas.^[123] The shorting pin can be equivalently modeled as an inductance and added in parallel to the resonant LC circuit of the patch.^[129] This makes the patch antenna resonate at a lower frequency and the sized reduction for the antenna can be obtained at a fixed frequency.

Table 3 illustrates various antenna types with their special geometry modifications, antenna characteristics and their simulation results, as well as the SAR values in the cardiac tissue.^[120,130–134]

In addition to the miniaturized planar-type antennas, significant efforts have been made in designing 3D conformal antennas that can be used as metal stents, thereby saving the additional volume of the antenna used for coronary stents. **Figure 5A–J** illustrates the planar antenna design of cardiovascular implants and the stent-based 3D conformal antenna design. For instance, Takahata et al.^[15] proposed a concept of a stent-based antenna (called “Stentenna”), which uses a stent as an antenna (or an inductor). It incorporates a capacitive pressure sensor to form an inductive-capacitor (LC) tank, which can be inductively coupled with an external antenna. This structure allows highly compact integration of antennas, stents, and biosensors. An extended study of the “Stentenna”^[16] led by this team designed a zigzag pattern without bridge struts in a stainless-steel tube, and then formed a helical structure when the tube is expanded, resulting in a significant increase of stent inductance (multiplied by a factor of 3.2). Moreover, a copper layer was covered on the stent owing to its high conductivity, thereby achieving a good resonance of the L-C circuit with a higher Q factor (35 at 150 MHz). In addition, the stent was further coated with a gold layer and a conformal parylene-C layer to guarantee the biocompatibility and electrical insulation of the stent antenna. This “Stentenna” promotes innovation from passive metal stents to compact and smart stents. In particular, Chen et al.^[135] reported the first attempt of a smart stent in the clinical setting, where the stent was deployed on a pig through a balloon catheter. The helical-structure stent is composed of an inductive stent and a capacitive pressure sensor, which provides an encouraging demonstration for wireless monitoring blood pressure in the vessel (a resolution of 12.4 mmHg) and also

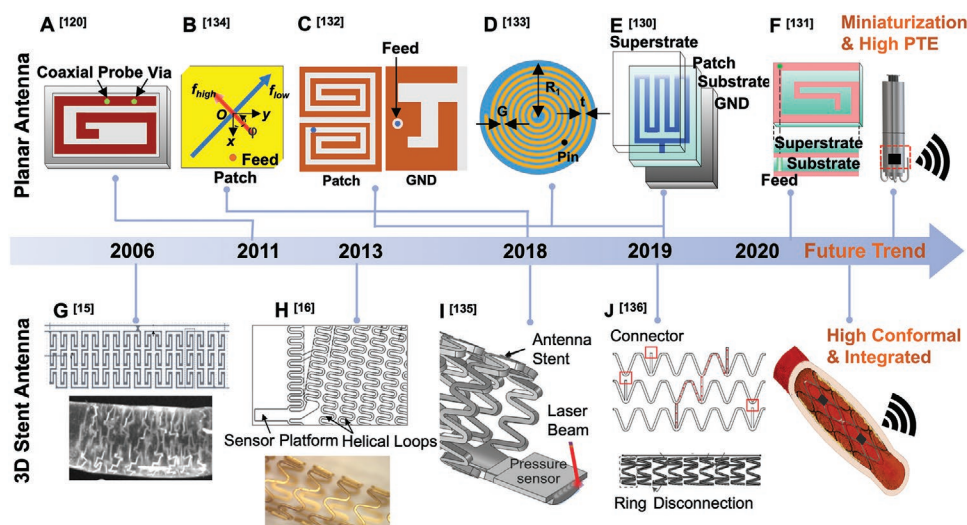


Figure 5. The timeline and categories of planar and 3D antenna design for cardiovascular implants: A) spiral-shaped microstrip patch antenna, B) microstrip patch antenna with two cutting diagonals, C) spiral-shaped antenna, D) spiral-shaped circular patch antenna, E) meander line patch antenna, and F) spiral-shaped patch antenna. G) This stent antenna comprises series of crossband and involute contours that connected to the longitudinal beam, H) the stent antenna arranged in angle bands in a zigzag pattern, showing a helical shape in 3D, I) helical structure stent antenna, and J) single-connector stent antenna. A) Reproduced with permission.^[120] Copyright 2011, Hindawi Publishing. B) Reproduced with permission.^[134] Copyright 2018, IEEE. C) Reproduced with permission.^[132] Copyright 2019, IEEE. D) Reproduced with permission.^[133] Copyright 2019, IEEE. E) Reproduced with permission.^[130] Copyright 2019, IEEE. F) Reproduced with permission.^[131] Copyright 2020, IEEE. G) Reproduced with permission.^[15] Copyright 2006, IEEE. H) Reproduced with permission.^[16] Copyright 2013, IOP Publishing. I) Reproduced under the terms of the CC-BY 4.0 license (<https://creativecommons.org/licenses/by/4.0/>).^[135] J) Reproduced with permission.^[136] Copyright 2019, Multidisciplinary Digital Publishing Institute.

meets the PCI standard procedure. In 2019, Liu et al.^[136] presented a stent antenna with good radiation performance. It consists of multiple rings connected by a single connector rather than a conventional multiconnector. Due to the random current distribution of the multiconnector stent antenna, the multiconnector stent antenna showed a higher resonant frequency than the single-connector antenna under the same dimension. This single-connector antenna achieved a S_{11} of -17 dB, a gain value of 1.38 dBi, and a radiation efficiency 74.5% at a resonant frequency of 2.07 GHz. In addition to EM-based antennas, acoustic wave-mediated magnetoelectric (ME) antennas have also emerged in recent years. Acoustic-based WPT is another branch of WPT, and it has also drawn considerable attention in powering implantable devices because it can realize ME antennas in nanoscale. Compared with EM-based WPT, which works on EM induction or EM radiation, the acoustic power transfer uses ultrasound waves or vibration to transmit energy. Particularly, acoustically driven nanomechanical ME antennas employ ferromagnetic/piezoelectric thin-film materials,^[137,138] and transmit energy through direct and converse piezoelectric effect and magnetostriction effect at the acoustic resonance frequency. Since the wavelength of the acoustic wave is shorter than the EM wave at the same frequency, these ME antennas enable to shrink 1–2 orders^[139,140] of magnitude miniaturization than the conventional laminate antennas, which greatly encourages the antenna miniaturization. However, the fabrication difficulty, low power levels, and high demands of materials (e.g., high piezomagnetic coefficient)^[141,142] are the main constraints currently faced for using ME antennas. Furthermore, the acoustic-based WPT is not the focus of this review paper, and we will introduce the EM-based WPT in detail in the rest of this section.

4.2. Specific Absorption Rate and Dielectric Properties in Human Tissue

The electromagnetic WPT system is based on the EM field to propagate energy from an external source to an internal implant. The attenuation of EM waves caused by tissue absorption will lead to non-negligible power loss and thermal effects. Therefore, the safety of human EM radiation is the primary concern of wireless power and data transmission in implantable devices. The power dissipation in WPT systems must comply with the safety regulations, in terms of SAR (W kg^{-1}) value, to avoid overheating of tissues/adverse health effect. SAR is defined as the EM energy absorbed by tissue per unit mass of tissue when exposed to EM radiation, which resulted in the tissue heat up^[143]

$$\text{SAR} = \frac{\sigma E^2}{\rho} \quad (6)$$

where E is the induced electric field, and σ and ρ are the conductivity (kg m^{-3}) and the mass density (S m^{-1}) of the tissue. In order to prevent the tissue from localized overheating, the SAR value must comply with the standards and guidelines of Federal Communications Commission ($\text{SAR}_{1g} \leq 1.6 \text{ W kg}^{-1}$ ^[144] and IEEE SAR safety standard ($\text{SAR}_{10g} \leq 2 \text{ W kg}^{-1}$ ^[145]). Moreover, the dielectric properties (permittivity and conductivity) of biological medium are significantly different from those in vacuum, resulting in a mismatch in EM waves propagation between the free space and biological medium. In addition, the SAR value is heavily affected by frequency.^[146] To select a proper operational frequency to minimize the power loss caused by the antenna-tissue interaction and simultaneously meet the SAR regulation,

Table 4. Dielectric properties of tissue layers at different operating frequencies.

Frequency	Tissue layer	Thickness [mm]	Conductivity [S m ⁻¹]	Relative permittivity
40.68 MHz ^[149]	Skin	–	0.38	124.3
	Muscle	–	0.67	82.6
	Fat	–	0.034	7.3
403.5 MHz ^[150]	Skin	3	0.68 (dry) 0.67 (wet)	46.71 (dry) 49.84 (wet)
	Fat	10	0.041	5.58
	Muscle	20	0.79	57.1
915 MHz ^[151]	Skin	–	0.74 (dry)	46.25 (dry)
1.427 GHz ^[152]	Fat	–	0.77 (wet)	44.03 (wet)
	Muscle	–	0.14	8.84
	Skin	–	0.70	53.83
	Muscle	–	1.04	39.6
2.4 GHz ^[153]	Skin	5	1.15	54.1
	Fat	10	1.46	38
	Muscle	10	0.11	5.3
3.5 GHz ^[154]	Skin	10	1.77	52.7
	Fat	2.5	2.35	41.41
	Muscle	5	0.42	10.5
10 GHz ^[155]	Skin	35	2.72	52.12
	Fat	–	8.01	31.29
	Muscle	–	0.58	4.62
	Muscle	–	10.62	42.76

the influence of EM radiation on the dielectric properties of biological tissue is worth investigating.

Permittivity, ϵ (F m⁻¹) (also known as dielectric constant), measures the ability of a substance to store electrical charges and is related to how well molecules of polarization under

a given applied electric field.^[147] In order to reduce the interference to the antenna radiation performance, a dissipative medium with a high dielectric constant is preferred. Relative permittivity determines as the ratio of a certain material's permittivity to the permittivity of vacuum ($\epsilon_0 = 8.85 \times 10^{-12}$ F m⁻¹) $\epsilon_r = \epsilon/\epsilon_0$. Conductivity, σ , represents the ability of a substance to carry charges, and it significantly affects the radiation efficiency, absorption cross-section, and stability of an antenna.^[148]

Significant efforts have been made to estimate the dielectric properties in human phantom models under different operating frequencies. **Table 4** summarizes the electrical properties with frequency changes in skin, fat, and muscle layers.^[149–155] This table indicates that the overall decreasing and growing trends of relative permittivity and conductivity change with increasing frequencies, separately. Therefore, it is pervasively agreed to select the optimal operational frequency at relatively low frequencies to maintain safe tissue absorption and minimal power loss. Furthermore, a charging control unit for reliable and safe charging of fully implantable medical systems is essential. In general, the control unit in WPT systems connects to charging circuit and the implantable device to coordinate the transmitted power and data. In particular, the power transmitted from the transmitter depends on the feedback of the receiver. For instance, when the transmitted power exceeds the power level required by the receiver, the transmitter will stop supplying power and enter a low-power standby mode.^[156]

In addition to the above discussion, this section also introduces the working principle of various WPT power links, antenna design, PTE, and advanced applications in cardiovascular implants. In general, WPT technology can be categorized into near-field, mid-field and far-field WPT according to its transmission distance and radiation mode. **Figure 6** illustrates different field regions of an antenna. The near-field region can be further divided into reactive near-field and radiative

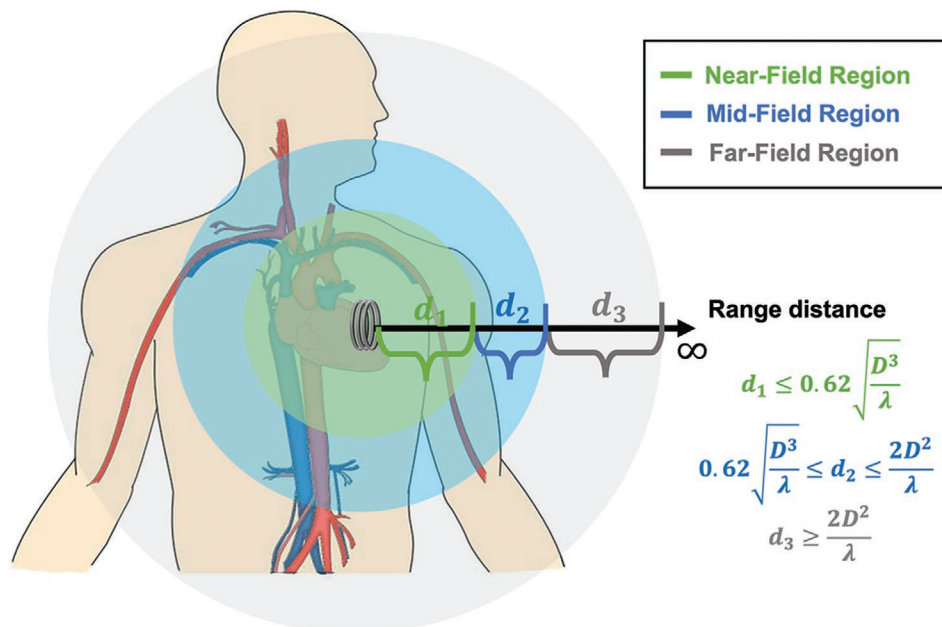


Figure 6. Field regions of wireless power transfer: d_1 : near-field region; d_2 : mid-field region; d_3 : far-field WPT transfer region.

near-field (Mid-range or Fresnel region). The transfer distance ranges of three fields are defined as follows^[157]

$$\text{Reactive near field } d_1 \leq 0.62 \sqrt{\frac{D^3}{\lambda}} \quad (7)$$

$$\text{Radiative near field } 0.62 \sqrt{\frac{D^3}{\lambda}} \leq d_2 \leq \frac{2D^2}{\lambda} \quad (8)$$

$$\text{Far Field } d_3 \geq \frac{2D^2}{\lambda} \quad (9)$$

where d is the radius of transmission region, D is the largest dimension of antenna, and λ is the wavelength.

4.3. Near-Field WPT

Near-field WPT has been widely used to transmit energy over short distances (limited to the range of millimeters (mm) and centimeters (cm)). Near-field WPT technology can be divided into three categories according to the working principle: inductive coupling, magnetic resonant coupling (MRC), and capacitive coupling (CC). Each scheme has its own merits and demerits, which will be discussed in detail. For instance, inductive coupling exhibits the highest power transfer efficiency, while magnetic resonant coupling possesses the largest transmission distance.

4.3.1. IC-WPT

Inductive coupling is the most established power scheme and has been extensively used in various wireless charging scenarios. It is a nonradiative technology that works in the near-field region based on the EM induction. A stable source supplies power and generates current in the transmitter coil (Tx), which induces a time-varying magnetic field between two coils (in the range of millimeter (mm) and centimeter (cm)), and then generates a voltage in the receiver coil (Rx). The IC-WPT exhibits remarkable high efficiency under the short distance and perfect alignment between Tx and Rx. The main factors that determine the PTE are the coupling coefficient “ k ” and the quality factor “ Q ” as shown in Equations (10)–(12)^[158]

$$k = \frac{M}{\sqrt{L_1 L_2}} = \frac{d_1^2 d_2^2}{\sqrt{d_1 d_2} (\sqrt{d_1^2 + D^2})^3} \quad (10)$$

$$Q = \frac{2\pi fL}{R_{\text{effective}}} \quad (11)$$

$$\eta = \frac{k^2 Q_1 Q_{2L}}{1 + k^2 Q_1 Q_{2L}} \cdot \frac{Q_{2L}}{Q_L} \quad (12)$$

where M is mutual inductance, and L_1 , L_2 are the self-inductance of a pair of coils separately. In the derived equation, d_1, d_2 are the diameter of the transmitter and receiver antenna, and D is the

separation distance. In Equations (11) and (12), L is the inductance and $R_{\text{effective}}$ is the self-resistance of antenna, Q_1 , Q_2 are the quality factor of two coils, $Q_{2L} = Q_2 Q_L / Q_2 + Q_L$, and $Q_L = R_{\text{LOAD}} / 2\pi f L_2$. The PTE of this power link is highly related to the size of the coils and the distance between the Tx and Rx coils. Although the inductive coupling presents a high PTE within the limited distance, the PTE is extremely sensitive to the distance limitation and precise alignment between Tx and Rx in the non-resonant state, which is known as weakly coupled (or loosely coupling). In particular, the intensity of the magnetic field is inversely proportional to the distance ($1/D^3$). Obviously, the PTE of inductive coupling attenuates significantly with the separation increase.

4.3.2. MRC-WPT

Inductive coupling exhibits a relatively high-power efficiency but hindered by short transmission distance and perfect coils alignment. If the separation distance between Tx and Rx exceeds this range or the coils are misaligned, the PTE will drop dramatically. Therefore, a strongly coupled MRC was initially investigated by Kurs et al.^[159] in 2007 to extend the transmission distance up to 2 m by introducing a four-coil WPT system. As illustrated in Figure 2H, the four-coil WPT system consists of a source coil, a transmitter coil, a receiver coil, and a load coil. In addition, external compensation capacitors are introduced to tune the resonant frequency of the resonant coils (Tx and Rx).^[160] Therefore, adjacent coils are coupled to each other through magnetic resonance coupling, which allows compensation of magnetic flux leakage to improve PTE with a longer transmission distance compared to the IC-WPT.

To guarantee the high PTE of MRC-WPT system, the consistency of resonance frequency is essential, as expressed in Equation (13)^[159]

$$f_r = \frac{1}{2\pi\sqrt{LC}} \quad (13)$$

where L and C are the self-inductance and parasitic capacitance of the resonant transmitter or receiver coils. In addition, the coils can be modeled by a series RLC circuit and the quality factor (Q) is given by Equation (14)^[161]

$$Q = \frac{2\pi f_r}{R} \quad (14)$$

where R is the parasitic resistance of the coils. Furthermore, the PTE is calculated based on the equivalent circuit, which is illustrated in the paper.^[162] The MRC-WPT system can be considered as a two-port network and the PTE of the wires power transfer system can be analyzed by scattering parameters S_{11} and S_{21} , as presented in Equations (15) and (16)^[162,163]

$$\eta = \frac{|S_{21}|^2 / Z_0}{\text{Re} \left[|S_{11} + 1|^2 / Z_{\text{in}} \right]} \quad (15)$$

where S_{11} is input reflection coefficient, $Z_0 = 50 \Omega$ is the characteristic impedance, Z_{in} is the input impedance, and S_{21} is the forward transmission coefficient can be expressed as follows

$$S_{21} = \frac{2k_{12}k_{23}k_{34}Q_2Q_3\sqrt{Q_1Q_4}}{1+k_{12}^2Q_1Q_2+k_{23}^2Q_2Q_3+k_{34}^2Q_3Q_4+k_{12}^2k_{34}^2Q_1Q_2Q_3Q_4} \quad (16)$$

where k_{12} (source to Tx), k_{23} (Tx to Rx), and k_{34} (Rx to load) are the coupling coefficient of adjacent coils, which can be found in Equation (10).

In general, two-coil and four-coil configurations are widely adopted by MRC-WPT systems.^[164,165] In the two-coil topology, the power source and the load directly connected to the Tx and Rx, eliminating the additional source and load coils. However, it has been demonstrated that the two-coil system exhibits lower tolerance with the distance and rotation variations compared to the four-coil configuration.^[166,167] For instance, a two-coil MRC system reported by Monti et al.^[168] delivered up to 1 mW power at a resonant frequency of 403 MHz to drive a pacemaker. In this study, a planar spiral-shaped resonator (SSR) and a square split ring-shaped resonator (SRR) were designed on Arlon 880 substrates served as the Tx and Rx, separately. Moreover, they also tested the sensitivity of the MCR link in terms of distance and misalignment. It shows that the PTE decreases rapidly as the distance exceeds 5 mm and the rotation angle is greater than $\pm 30^\circ$. In addition, Yellappa et al.^[169] reported a four-coil MRC-WPT system for biomedical implantation. They designed the circular and spherical shape coils and compared their performance in the case of lateral and angular misalignment. The external coils and implantable coils are fixed at an initial distance of 10 mm initial distance, the PTE is 78.5%. Then the coils moved to 40 mm and the rotation changed from 0° to 90° . The PTE of the four-coil configuration is robust within 15 mm and up to 50° of angular misalignment. In general, the results verified that the spherical shape coil presents a higher tolerance with overall misalignment than the circular coil.

Although aligning the coils can maximize the coupling between the coils, it is usually not possible in biomedical implants. For example, blood flow and body motion can affect the position of internal coil. Compared with the inductive coupling, the MRC-WPT scheme can mitigate the interference induced by the misalignment over a longer transmission distance. The four-coil structure MRC is preferable by adding the extra high Q resonant coils, which is strongly coupled to the source and load coils. However, the four-coil configuration contributes to the volume of the WPT system, causing the burden for implantation in the body. In addition, the phenomenon of frequency splitting of both two-coil and four-coil structures can lead to a high PTE but low load power at the resonant frequency.^[161,170]

4.3.3. CC-WPT

Capacitive coupling WPT uses one or two pairs of parallel conductor plates to instead of coils as the Tx and Rx.^[171] This scheme uses induced displacement current as the carrier, which is derived from the electric field (compared to the magnetic field of the inductive coupling) between the conductor plate pairs to achieve wireless power delivery.^[172] Therefore, CC-WPT profits from a lower EM interference and a higher misalignment tolerance compared with the inductive coupling.^[171,173] The most common CC-WPT system requires two metal plates

as Tx, and the other two served as Rx to form a coupling capacitor separating by a medium to provide a power flow loop (to form receive and return paths of the displacement current), and then connect to an alternating current (AC) source and a load, separately. In this approach, the coupling capacitor (similar to the Q factor in the inductive coupling) plays a vital role in the amount of power transfer. The equations of coupling capacitance and displacement current are defined as Equations (17) and (18)^[172,174]

$$C_T = \epsilon_0 \epsilon_r(\omega) \frac{A}{D} \quad (17)$$

$$I_{\text{disp}} = \epsilon_0 \epsilon_r(\omega) A \frac{\partial \vec{E}}{\partial t} \quad (18)$$

where ϵ_0 , $\epsilon_r(\omega)$ are the free space permittivity and frequency variant permittivity, A is the effective area, and D is the separation between the plates, and $\frac{\partial \vec{E}}{\partial t}$ is the rate of the electric field delay. The power loss in capacitive coupling includes tissue loss, conduction loss, and source loss. Among them, the conductive loss and source loss are much smaller than the tissue loss and can be ignored when operating in MHz to GHz range. Therefore, the tissue loss can be quantified as equivalent to resistance, and the PTE of a capacitive coupling link is defined as Equation (20)^[175]

$$R_T = \text{Real} \left(\frac{-jD}{\omega \epsilon_0 \epsilon_r(\omega) A} \right) \quad (19)$$

$$\eta = \frac{R_L}{R_L + R_T} (1 - |\Gamma|^2) \quad (20)$$

where R_L is the load resistor and Γ is the reflection coefficient.

However, the value of coupling capacitance is constrained by the size of conductor plates and the small ϵ_0 value ($\epsilon_0 = 8.85 \times 10^{-12} \text{ F m}^{-1}$). Moreover, when designing the CC-WPT link to realize the optimal PTE, a trade-off between parameters A , D , and operational frequency need to be considered. Due to the low coupling capacitance and short transmission range (in the millimeter range), a resonant compensation network (including capacitors and inductors) is commonly required to resonate with the coupler and boost the power transmission.^[176,177]

Due to the limited conditions and performance of CC-WPT, it has not been widely investigated in the application of biomedical implants. Early research on capacitive coupling in implantable medical systems started in 2009.^[173] It listed several advantages of capacitive coupling over inductive coupling (e.g., low EM interference and high immunity with misalignment^[178]) in biomedical applications, and also presented a design of power and data telemetry link for biomedical implants. However, this scheme is constrained by the bulky volume (e.g., four-plate structure) and low power output. For instance, Aldaoud et al.^[40] tested both inductive and capacitive power links for powering stents in vitro. The result shows that the overall PTE of inductive coupling is higher than its capacitive coupling counterpart.

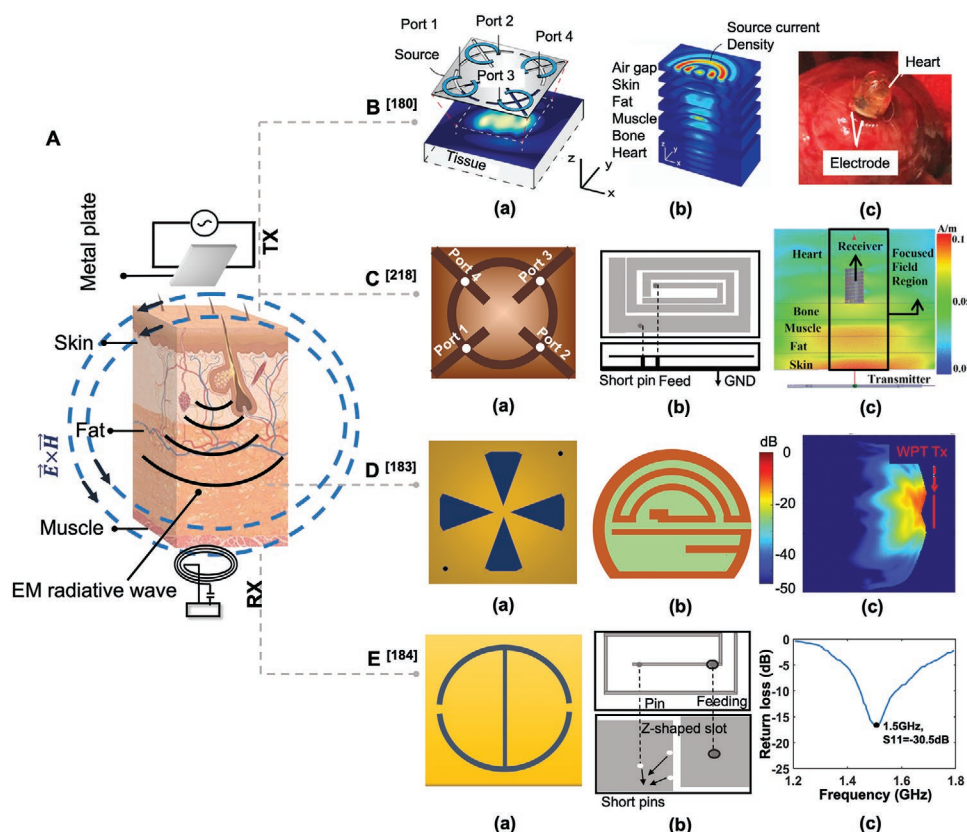


Figure 7. The working principle of mid-field wireless link and its applications in cardiovascular implants: A) work principle of mid-field WPT. B-a) Scheme of mid-field source (metal plate), b) magnetic field distribution in multitissue layers, and c) its application in powering electrostimulator implanted in a rabbit. Reproduced with permission.^[180] Copyright 2014, Proceedings of the National Academy of Sciences of the United States of America. C-a) Mid-field transmitting antenna, b) spiral type implanted antenna, and c) antenna measurement set up. Reproduced with permission.^[218] Copyright 2015, IEEE. D-a) Mid-field transmitter, b) quad-band implantable antenna, and c) The SAR distribution of Tx at 1470 MHz. Reproduced with permission.^[185] Copyright 2020, IEEE. E-a) Transmitting antenna, b) PIFA implanted antenna, and c) simulation result of return loss. Reproduced with permission.^[184] Copyright 2020, IEEE.

4.4. Mid-Field WPT

The mid-field WPT offers an innovative solution for powering over a longer range at a higher frequency (low GHz range) than the reactive near field coupling methods through a hybrid induction mode (external) and radiation mode (internal). Mid-field WPT benefits from a patterned metal plate with four ports to generate an ideal field pattern. By manipulating the ports, the metal plate can induce concentrated and adaptive energy transmission in deep tissue through the exponential decay of the magnetic field in the propagation mode.^[179,180] Particularly, the four ports of the patterned metal plate are excited by four independent phased RF signal, which is used to operate the focused region of the field and further improve the efficiency. As depicted in **Figure 7A**, the patterned metal plate is placed near the air–skin interface, and then the output field can be concentrated in small ranges (less than the vacuum wavelength), thereby generating a high energy density region.^[180]

The overview of SAR, dielectric properties and frequency in the previous section indicates a general concept that low frequencies are more suitable for WPT propagation in biological tissues. However, by employing a full wave analysis of WPT in implantable devices, it has been proved that the optimal frequency of

miniaturized coils (in the range of millimeter or micrometer) is in the GHz range, as presented in Equation (21)^[181]

$$f_{\text{opt}} \approx \frac{1}{2\pi} \sqrt{\frac{c\sqrt{\epsilon_0}}{\tau d(\epsilon_0 - \epsilon_\infty)}} \quad (21)$$

where c is speed of light, ϵ_0 , ϵ_∞ , τ are the dielectric properties of tissue in the Debye relaxation model, d is the distance between Tx and Rx. Compared with the most common WPT in the KHz or MHz range, this method can dramatically shrink the size of the receiver coil by 10^4 times due to its higher operating frequency (midfield).^[181]

Mid-field WPT is preferable for powering deep tissue (>5 cm) implants, especially for cardiovascular implants, which has motivated many researchers to contribute to this promising approach. For instance, Ho et al.^[180] demonstrated the feasibility of mid-field WPT in powering implantable devices, as shown in **Figure 7B-a,b,c**. The small receiver coil (2 mm in diameter) in the heart received 195 μW of power from 500 mW input power and spaced at least 5 cm apart. Later on, Das et al.^[182] applied the mid-field WPT technique in powering a leadless pacemaker at the optimal frequency 1.5 GHz (derived by calculating formula

(21) by using heart tissue). The mid-field transmitter antenna was designed as a slot array-like metal plate based on a Teflon substrate, and a spiral-shaped PIFA antenna (Rx) was fabricated on a flexible polyamide substrate, as shown in Figure 7C-a,b,c. Under the mid-field WPT system, they delivered 500 mW power at Tx and received 2.9 mW power at Rx, which is sufficient for most cardiovascular implants. Recently, Basir and Yoo^[183] proposed an efficient WPT system based on the mid-field technique for deep-body implants. The proposed configurations of Tx and Rx are shown in Figure 7D-a,b,c. The mid-field transmitter constructed a slotted structure and four ports on Teflon substrate to efficiently concentrate the power in the tissue through appropriate phase control. Meanwhile, the authors developed a compact implantable antenna with a spiral-shaped structure that supports quad-band operation. From their measurement results, the system can deliver 6.7 mW power for deep tissue implants over 5 cm, which shows great potential of powering the cardiovascular implants. Subsequently, Nguyen et al.^[184] reported a compact mid-field Tx configuration to power miniature implants, as presented in Figure 7E-a,b,c. A planar PIFA type antenna with a Z-shaped slot (on the ground layer) and three short pins was used for the Rx (with a size of $9 \times 13 \text{ mm}^2$) to achieve the maximum gain value. This mid-field WPT system operates at an optimal frequency of 1.5 GHz and shows a highly concentrated magnetic field in the tissue by observing the current density and the magnetic field. The Rx was placed in a heart tissue layer 55 mm away from the Tx, and 5.6 mW of output power was measured at the Rx from 1 W power coupled to the Tx. In addition, they tested the performance of the mid-field WPT under various misalignment conditions (lateral and angular misalignment). Consequently, the interference caused by the misalignment can be basically elimi-

nated under the mid-field WPT according to the stable S_{21} value and PTE with all misalignment cases, which is an encouraging solution for implantable devices.

Mid-field WPT provides a prominent strategy that is more suitable for powering cardiovascular implants than other conventional near-field WPT schemes. It surpasses the limitations of short transmission distance and misalignment. Meanwhile, the controllable metal plate can adjust the magnetic field pattern in tissues to increase the PTE. In addition, this approach promotes the miniaturization of implantable receivers in the low GHz range.

4.5. Far-Field WPT

Far-field WPT/far-field RF refers to the power that can be transmitted by laser beams or microwaves^[185] based on EM radiation. The propagation of EM radiation from the Tx to the Rx in a far field WPT system is depicted in Figure 8A.^[186]

In contrast, the transmission power attenuates rapidly as the distance between Tx and Rx increases in the near-field coupling, while the beam of far-field WPT can radiate a long distance (in the range of meters). Nevertheless, a long transmission distance will cause significant path loss, resulting in low power transfer efficiency. This is the major drawback of far-field WPT due to the energy transmitted by EM waves radiates and dissipates in all directions.^[187]

The architecture of an end-to-end far-field power link is presented in Figure 8B,^[188] which includes several energy-conversion processes: direct current (DC) to RF conversion (P_{Tx}), effective radiative power from Tx (P_{in}), free-space transmission (P_{inc}), incident power from Rx (P_{Rx}), and RF to DC

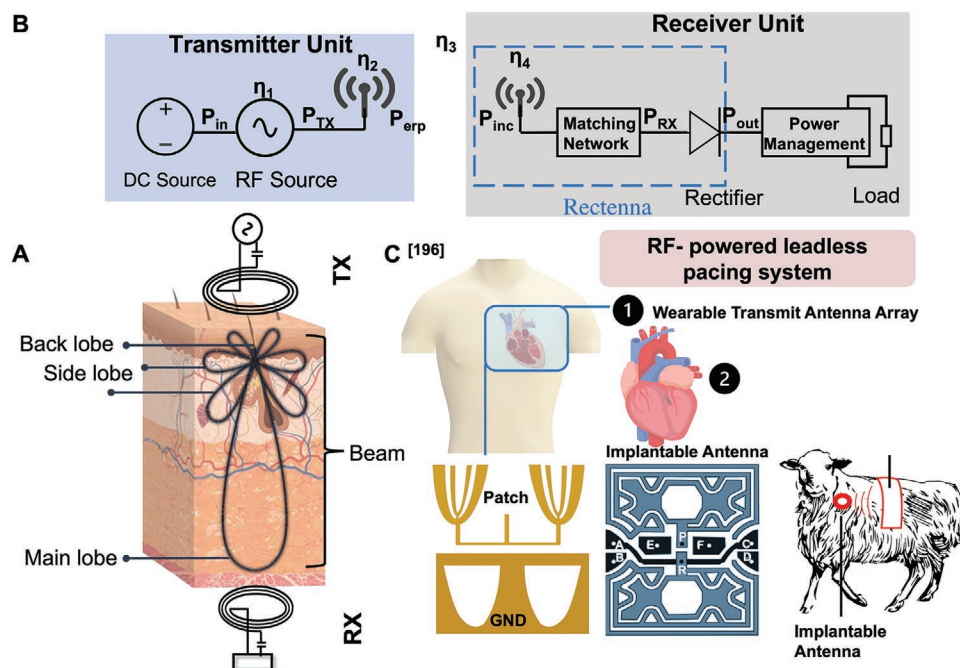


Figure 8. The working principle of far-field radiation and its application in cardiovascular implants: A) the work principle of far-field radiation. Adapted with permission.^[1] Copyright 2020, Wiley-VCH. B) End-to-end power link of far-field WPT, where $\eta_1 \times \eta_2$ is the transmit efficiency, $\eta_4 \times \eta_5$ is the receive efficiency, and η_3 is the free-space propagation efficiency. C) RF-powered leadless pacing system with a wearable transmit-antenna array, an implantable rectenna, and its animal experiment in an ovine. Adapted with permission.^[196] Copyright 2018, IEEE.

conversion (P_{out}). Therefore, the overall power transfer efficiency is presented as Equation (22)^[188]

$$\eta = \frac{P_{\text{out}}}{P_{\text{in}}} = \frac{P_{\text{TX}}}{P_{\text{in}}} \frac{P_{\text{erp}}}{P_{\text{TX}}} \frac{P_{\text{inc}}}{P_{\text{erp}}} \frac{P_{\text{RX}}}{P_{\text{inc}}} \frac{P_{\text{out}}}{P_{\text{RX}}} = \eta_1 \eta_2 \eta_3 \eta_4 \eta_5 \quad (22)$$

The PTE of far-field WPT is hindered by multipath loss. In particular, the transmit efficiency ($\eta_1 \times \eta_2$) and the receive efficiency ($\eta_4 \times \eta_5$) are of great significance to the optimization of PTE in the far-field WPT. Regarding the transmit efficiency, directional antennas or antenna arrays can be employed to mitigate the path loss by accurately concentrating the EM radiation to the targeted receiver.^[189] The antenna array with beam steering characteristics can manipulate the beam pattern to achieve a directional main lobe with low side lobes, thereby enhancing the directivity.^[190] When receiver antenna receives the radiated RF power, it will pass through the rectifier circuit and converts it into the DC power to the load. Therefore, an efficient “rectenna” (combined antenna and rectifier circuit) is also crucial for improving the receive efficiency, especially for converting RF to DC.

The first far-field wireless microwave transfer was demonstrated by Brown in 1964.^[191] It utilized a rectenna to receive microwaves to drive a model helicopter. In the past few years, extensive work has been done in investigating and designing high-performance rectenna.^[192,193] Particularly, it is recommended to use circularly polarized (CP) antennas to solve the polarization mismatch and multipath reduction issues.^[194] When the rectenna rotates, the output DC voltage will not be affected too much due to the circular polarization allows the rotation of the circuit.^[195] Therefore, the CP antenna overcomes the misalignment issue between Tx and Rx.

In recent years, RF-based far-field power strategies have aroused great interest in wearable and implantable devices with the Internet of things (IoT) medical systems. For instance, the paper^[196] proposed an RF-powered leadless pacing system with a wearable transmit-antenna array and an implantable rectenna (Rx), as shown in Figure 8C. They adopted a planar dipole antenna with a fractal geometry as the receiver and fabricated it on a Rogers TMM10i substrate ($\tan \delta = 0.002$, $\epsilon_r = 9.8$), and then matched it with a modified-Greiner rectifier circuit. The efficient transmit array based on the RT/Duroid 6010 (thickness of 0.254 mm) was designed with two semioval shaped truncations in the ground plane to realize the directional beam of the antenna. As a result, the overall wireless pacing system was successfully verified in an ovine model in vivo, and finally achieved 65% of PTE at operating frequency of 954 MHz. Another work in the study of far-field RF powered leadless pacemaker was developed by Abdi and Aliakbarian.^[197] The rectenna system consists of a CP spiral PIFA antenna and a single-diode detector based on Schottky diodes, and then measured in a three-layer tissue model. This system achieved a 40% RF-DC power conversion efficiency and measured a 0.2 V DC output voltage from an input power level of -20 dBm.

Compared with near-field WPT, far-field WPT significantly enhances the flexibility in Tx/Rx distance and movement. However, safety issues caused by RF exposure and the low

efficiency caused by the polarization mismatch and multipath are the main concerns of far-field WPT.

For safety reasons, the RF-based far-field WPT should operate in the low frequency range with high PTE. In addition, the PTE of far field RF can be improved by the DC to RF, RF to RF, and RF to DC subsystems. In particular, the CP beam-steering antenna array and efficient rectenna circuit are the directions that should contribute to the future. In summary, a comprehensive comparison of the state-of-the-art WPT system along with the characteristics of transceivers, power specification, and transfer distance, is presented in Table 5.

5. Bidirectional Wireless Data Transfer and Communications

The wireless power link is the premise of continuously performing the functions of biomedical implants. In addition, patients with chronic cardiovascular diseases require long-time physiological data monitoring and therapy. Hence, the wireless link is also essential in carrying bidirectional data for the communication between internal implants and external systems. The aforementioned wireless links for powering are available for data transmission as well. Presently, near-field communication is dominant in wireless data transfer (e.g., near field communication (NFC)) due to its lower power loss and higher safety when interacting with the human tissue.

Wireless data communication in IMDs has been developed to control and collect the biological data from the implantable devices to external systems, a bidirectional wireless data link for cardiovascular implants is presented in Figure 9.^[198] Implantable biosensors can detect and collect specific biological signals through sensing electrodes. However, the collected signal is weak and noisy, so it needs to be postprocessed through an amplifier and a filter to adjust its amplitude and remove the noise from the biological signal. The amplified signal is then interfaced to an analog-to-digital converter (ADC), which is used to convert the signal to a digital signal. The digital signal is further sent to a DSP processor, and then transmitted to the external system by using an appropriate modulation scheme.

In general, the data link can be divided into uplink (back telemetry) and downlink (forward telemetry). In implantable biomedical systems, the physiological data feedback from internal implants to the external unit is defined as uplink, and the data sent from outside system to internal implants to control the device is defined as downlink. In particular, the carrier data of uplink and downlink are transmitted through modulation and demodulation technique.

With the rapid advancement in wireless links and biomedical implants, wireless power and data systems are expected to be applied to the monitoring and treatment of cardiovascular implants. However, achieving simultaneous high PTE and high data rates over a single link is a major challenge of the near field scheme. In general, low operating frequencies (MHz range) are preferable since the fewer losses and higher efficiency in the near-field link. Nevertheless, compared to higher frequencies, lower frequencies generally have a narrower bandwidth, which limits the channel capacity and data rate. In addition, high data rates usually require high power consumption,

Table 5. Comparison of the state-of-the-art WPT systems for cIMDs.

Refs.	WPT technique	Operation frequency	Transfer distance [mm]	Tx			Rx			PTE
				Type	Dimension	Power	Type	Dimension	Received power	
[180]	Mid-field	1.6 GHz	>50	Patterned metal plate	2 mm diameter	500 mW	Coil	6 × 6 cm	195 μW (for heart)	–
[193]	Far field	2.45 GHz	500	Patch	–	1 W	PIFA	4 × 8 × 1.27 mm ²	<–22.5 dBm	–
[168]	MCR	403 MHz	5	Spiral resonator	30 × 30 × 0.508 mm ³	80 mW	Square SSR	14.9 × 14.9 × 0.508 mm ³	1 mW	5.24%@1 cm
[182]	Mid-field	1.5 GHz	55	Slot array-like metal plate	63 × 63 × 1.6 mm ³	500 mW	Spiral-shaped PIFA (patch)	20 × 30 × 0.05 mm ³	2.9 mW	0.59%
[40]	Inductive coupling	4 MHz	>30	Coil	100 mm (diameter) 70 mm (length)	500 mW	Coil	4 mm diameter 40 mm length	–	2.25% (peak value)
	Capacitive coupling	200–400 MHz	15 and 30	Two conductor plates	100 mm (diameter) 70 mm (length)	53 mW	Coil	4 mm diameter 40 mm length	–	2.6%@15 mm 1%@30 mm
[194]	Far-field	915 MHz	0.4 m	Patch with four metal pins	130 × 130 mm ² (patch)	25 dBm	Patch	11 × 11 × 1.27 mm ³	5.14 μW	–
[183]	Mid-field	1.47 GHz	50	Slotted metal plate	6.3 × 6.3 × 1.6 mm ³	1 W	Meander-line patch	8.43 mm ³	6.7 mW	0.67%
[184]	Mid-field	1.5 GHz	55	Slotted metal plate	65 × 65 × 2 mm ³	1 W	PIFA	9 × 13 × 0.8 mm ³	5.6 mW	0.56%

which rapidly depletes the energy of the entire wireless link. Alternatively, multiple dedicated wireless links (multicarrier) have been proposed to separate the power and data transmission links to achieve their respective goal.^[199] However, the multicarrier will introduce multiple coils, leading to complicated link design, space occupation, and crosstalk between links.^[200] From this perspective, compared with the multicarrier, the single carrier profits from better robust coupling thus realizing more reliable data transmission.^[201] Moreover, appropriate modulation/demodulation technique over a single link may resolve the conflict between power and data link requirements. In particular, a suitable modulation/demodulation scheme can offer high reliability and low power consumption on the datalink by reducing the data error rate and power dissipation.^[202] In this section, we will introduce and review the fundamentals of various modulation/demodulation schemes for uplink and downlink communications and their applications in cardiovascular implants.

5.1. Downlink Data Transmission

Modulation is the process of impressing information from an input signal into a carrier signal by modifying the carrier signal parameters (such as frequency, amplitude, and phase), while demodulation is used to extract information from the carrier signal or recover the original signal.^[202] Presently, various modulation and demodulation techniques have been widely used to perform downlink data transmission from external devices to wireless implants (such as amplitude-shift keying (ASK), frequency-shift keying (FSK), phase-shift keying (PSK), and their derivatives). An ideal modulation scheme for wireless implants should have the characteristics of high data rate, low power consumption, low bit error rate (BER), and narrow bandwidth.^[203]

However, each type of modulation has its advantages and disadvantages, it is necessary to select the appropriate modulation method according to the specific requirements. ASK or its variant on/off keying (OOK) modulation/demodulation scheme is most commonly used for wireless implants because of its simple architecture and low power consumption.^[200] Nevertheless, the evident drawback of this linear scheme is vulnerable to noise due to the carrier amplitude is easily corrupt by the interference.^[204] Therefore, the probability of BER in OOK is higher than that of FSK and PSK,^[203] where BER is defined as the ratio of the number of bit errors to the total received bits. The noise immunity of a data link is measured by BER versus signal-to-noise ratio (SNR). FSK technique is suitable for sending binary data with two carrier frequencies.^[205] In particular, FSK benefits from better noise immunity, but it subjected to limited data rate and larger bandwidth occupation.^[206] Alternatively, PSK also exhibits less susceptibility to noise for a given SNR and is more power-efficient than ASK.^[203] In PSK modulation, the phase of the carrier is modulated to represent the binary data. Among various variants of PSK, binary-PSK (BPSK) is the simplest scheme. For instance, Hu and Sawan^[207] employed a fully integrated BPSK as a demodulator in the inductive coupling link of IMDs, with a power consumption of 0.7 mW and a data transmission rate of 1.12 Mbps. To achieve higher data rates, other PSK-variants (such as quaternary-PSK(QPSK),^[208] offset-QPSK(OQPSK),^[209] differential PSK (DPSK),^[210] and high-order PSK methods) have been investigated in biomedical applications.

5.2. Uplink Data Transmission

Uplink data transmission is used to record the parameters in-body and transmit data to the external unit. In particular, the

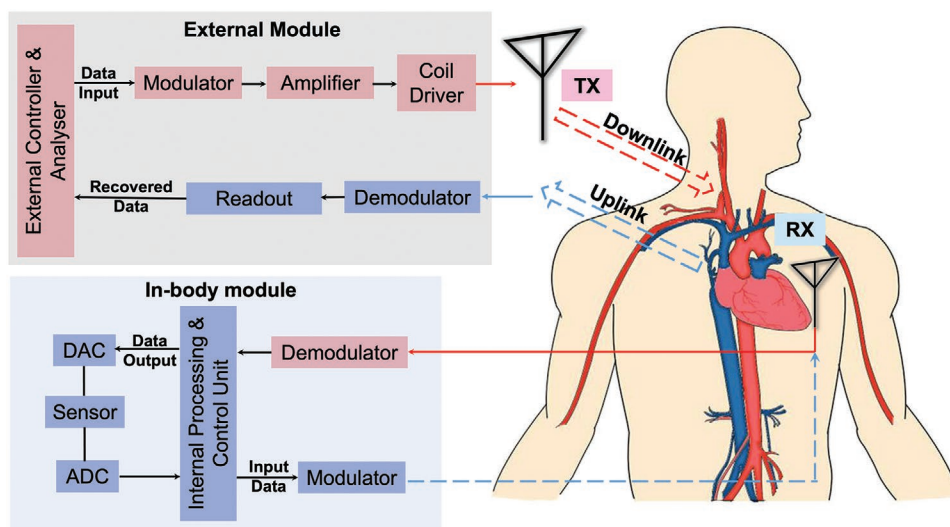


Figure 9. A bidirectional wireless data link for cardiovascular implants.

most extensively employed passive impedance modulation for uplink data transmission is load shift keying (LSK). The LSK uses an on-off switch to change the load impedance of the implant to transmit data. The change of load impedance will induce the current changes in the implantable circuit, and further cause the current change of the external circuit on the inductive link.^[211] Nevertheless, when the weak coupling occurs (coupling coefficient (k) = 0.01 in general),^[212] this modulation exhibits low reliability. In addition, the mistuning on/off state of LSK^[213] will reduce the PTE of power transmission. Owing to that, an advanced alternative solution called passive phase shift keying (PPSK) has been proposed^[214] to address the above shortcomings of LSK modulation. The PPSK uses a similar circuit design to the LSK, but is distinguished by its more accurate state (on/off) operation than the LSK, which enables a rapid transient response according to impedance change.^[215] In particular, Jiang et al.^[215] reported a PPSK modulator for biomedical implants, using a 13.56 MHz carrier frequency under the weak coupling condition to achieve a data rate of 1.35 Mb s⁻¹ and a BER of less than 1×10^{-5} for uplink data transmission. They also verified the effect of PTE with the PPSK and showed that the PTE was only reduced by 6% PTE when PPSK modulation was applied. In addition, cyclic on-off keying (COOK) modulation is another substitute that presents a higher data rate than LSK and PPSK. The COOK scheme is prominent in introducing a shorting switch on the LC tank, and it only takes one single cycle to close the switch, thereby achieving a high data rate.^[216] In addition, the COOK synchronous short circuit does not affect the resonance effect or reduce power loss. For example, Ha et al.^[216] verified the performance of COOK modulation to simultaneously achieve efficient power transfer (maximum 89.2%) and high data rate (6.78 Mb s⁻¹) on a single 13.56 MHz link.

Considering the reliability, simplicity and size constraints, the single link is preferable for simultaneous power and data transmission. However, achieving high effectively bidirectional transmission is the main challenge in developing and exploiting appropriate modulation/demodulation technique.

6. Conclusion and Future Direction

Long-term implantation of biomedical devices is indispensable for chronic cardiovascular patients to regulate or replace the abnormal or missing functions in the body. Wireless and battery-free power technologies allow the support for noninvasive devices for diagnostic and therapeutic purposes without repeated surgical procedures, a comprehensive comparison of all the battery-less power strategies for cIMDs is presented in Table 6. Particularly, energy harvesting technologies have emerged to collect the dissipated energy in the human body or ambient to realize self-powered implants. These energy transducers based on advanced flexible materials have been tested in animals to prove the feasibility of powering low power cIMDs. In particular, energy from the cardiovascular system is considered to be an ideal source that can directly power cardiovascular implants through PENGs or TENGs. However, the output of biochemical and mechanical energy in the body cannot satisfy the power requirement of the cardiovascular implants with relatively high-power dissipation, such as smart stents. Moreover, an additional data transmission system needs to be constructed to record the internal conditions of the cardiac, resulting in additional circuits and unwanted percutaneous wires.

Instead of passively harvesting energy, EM-based wireless transfer systems are expected to eliminate batteries and percutaneous wires over a single link that can guarantee a continuous and noninvasive operation of the cardiovascular implants. In addition, WPT is designed to provide a stable and controllable wireless power supply from the external transmitter unit. However, the inductive coupling WPT suffers from the short transmission distance and poor misalignment tolerance, resulting in weak coupling. Although magnetic resonant coupling exhibits higher immunity against the misalignment and achieves a longer distance by introducing tuning resonant circuits, the complex circuitry design and large occupation of implantable circuits hindered its application in biomedical implants. Furthermore, far-field RF suffers from side effects of

Table 6. Comparison of battery-less power strategies for cIMDs.

Energy harvesting type	Technique	Elements	Materials	Generated power/energy level	Merit	Demerit
In-body energy harvest	Biofuel cells	Electrode	Ag/Pt/Au/CNTs	Output voltage <1 V	<ul style="list-style-type: none"> ● Biocompatible ● Abundant fuels in the body 	<ul style="list-style-type: none"> ● Low output voltage ● Low conversion efficiency
	Piezoelectric transducer	Cantilever beam Piezoelectric film	Ceramic materials Polymers Composite materials/ nanomaterials	Power density in the range of $\mu\text{W cm}^{-3}$ and mW cm^{-3}	High energy density	<ul style="list-style-type: none"> ● Complex structure and circuitry ● Affected by the vibration frequency
	Triboelectric transducer	Triboelectric material pair	Two materials with strong electron affinity	Power density $\mu\text{W cm}^{-3}$ level	<ul style="list-style-type: none"> ● Simple construction ● Easy fabrication 	Low energy densities
	Thermoelectric transducer	Thermocouple	Semiconductors/conductive polymer/hybrid materials	Power density $\mu\text{W cm}^{-3}$ level	<ul style="list-style-type: none"> ● No moving component ● Long-term energy supply 	<ul style="list-style-type: none"> ● Low conversion efficiency ● Time-variant temperature difference required in the body ● Limited implantable locations
External wireless power transfer	Inductive coupling	Coil	Aluminum/copper/iron	Output power Consider the SAR limitation, size, distance: in the range of μW to mW	High transfer efficiency	<ul style="list-style-type: none"> ● Short transmission distance (cm) ● Accurate alignment requirement
	Capacitive coupling	Conductive plate	Conductor materials		Nonradiative	Very short distance (mm)
	Magnetic resonant coupling	Resonator	Aluminum/copper/iron		Medium transmission distance (m)	Multiple coils occupied space
	Mid-field	Antenna	Patterned metal plate (Tx)		Efficiently concentrate the power in the tissue, high tolerance with alignment	–
	Far-field	Antenna	Depends on the substrate		Long transmission distance (m)	Low efficiency

low efficiency and localized heating in the body caused by the multipath absorption and scattering.

Consequently, mid-field WPT has marvelous potential in power solutions for deep cardiovascular implants. It manipulates the EM field to be concentrated in the tissue through a patterned metal plate, thereby generating a high energy density region and further enhancing the PTE. In addition, compared with the near field WPT, the mid-field WPT addresses the interference induced by misalignment and extends the transmission distance. Furthermore, due to its optimal frequency in biological tissues in the sub-GHz range, this solution also promotes the miniaturization of the antenna.

In terms of data transmission, advanced modulation/demodulation technology is a breakthrough to realize high power and high data rates with low BER over a single link. In particular, the COOK scheme has the potential to allow high data rates and minimize power loss. By further research on wireless power and data transfer technique under safety regulations, fully wireless and battery-free cardiovascular implants are thriving and can be realized in the near future.

Conflict of Interest

The authors declare no conflict of interest.

Keywords

cardiovascular implantable medical devices, energy harvesting strategies, power supply solutions, wireless power and data transmission

Received: August 24, 2021
Revised: November 20, 2021
Published online: January 7, 2022

- [1] J. Zhao, R. Ghannam, K. O. Htet, Y. Liu, M.-k. Law, V. A. Roy, B. Michel, M. A. Imran, H. Heidari, *Adv. Healthcare Mater.* **2020**, *9*, 2000779.
- [2] A. Pfenniger, M. Jonsson, A. Zurbuchen, V. M. Koch, R. Vogel, *Ann. Biomed. Eng.* **2013**, *41*, 2248.
- [3] N. Li, Z. Yi, Y. Ma, F. Xie, Y. Huang, Y. Tian, X. Dong, Y. Liu, X. Shao, Y. Li, *ACS Nano* **2019**, *13*, 2822.
- [4] H. Zhang, X.-S. Zhang, X. Cheng, Y. Liu, M. Han, X. Xue, S. Wang, F. Yang, A. Smitha, H. Zhang, *Nano Energy* **2015**, *12*, 296.
- [5] A. Nozariasbmarz, R. A. Kishore, B. Poudel, U. Saparamadu, W. Li, R. Cruz, S. Priya, *ACS Appl. Mater. Interfaces* **2019**, *11*, 40107.
- [6] D. Vervoort, B. Meuris, B. Meyns, P. Verbrugghe, *J. Thorac. Cardiovasc. Surg.* **2020**, *159*, 987.
- [7] N. Van Hemel, E. Van der Wall, *Neth. Heart J.* **2008**, *16*, S3.
- [8] M. Carrión-Camacho, I. Marín-León, J. M. Molina-Doñoro, J. R. González-López, *J. Clin. Med.* **2019**, *8*, 35.

- [9] S. Burkhard, V. Van Eif, L. Garric, V. M. Christoffels, J. Bakkers, J. *Cardiovasc. Dev. Dis.* **2017**, *4*, 4.
- [10] K. Kaszala, K. A. Ellenbogen, *Circulation* **2010**, *122*, 1328.
- [11] A. F. Stephens, A. Busch, R. F. Salamonsen, S. D. Gregory, G. D. Tansley, *IEEE Trans. Control Syst. Technol.* **2020**, *29*, 1009.
- [12] L. Brancato, G. Keulemans, T. Verbelen, B. Meyns, R. Puers, *Micromachines* **2016**, *7*, 135.
- [13] J. Vishnu, G. Manivasagam, *Med. Devices Sens.* **2020**, *3*, e10116.
- [14] D. Hoare, A. Bussooa, S. Neale, N. Mirzai, J. Mercer, *Adv. Sci.* **2019**, *6*, 1900856.
- [15] K. Takahata, Y. B. Gianchandani, K. D. Wise, *J. Microelectromech. Syst.* **2006**, *15*, 1289.
- [16] A. R. Mohammadi, M. S. M. Ali, D. Lappin, C. Schlosser, K. Takahata, *J. Micromech. Microeng.* **2013**, *23*, 025015.
- [17] M. Cai, K. Takahata, S. Mirabbasi, in 2020 18th IEEE Int. New Circuits and Systems Conf. (NEWCAS), IEEE, Piscataway, NJ **2020**.
- [18] D. Son, J. Lee, D. J. Lee, R. Ghaffari, S. Yun, S. J. Kim, J. E. Lee, H. R. Cho, S. Yoon, S. Yang, *ACS Nano* **2015**, *9*, 5937.
- [19] S. Y. Chair, D. S. Yu, M. T. Ng, Q. Wang, H. Y. Cheng, E. M. Wong, J. W. Sit, *J. Geriatr. Cardiol.* **2016**, *13*, 425.
- [20] G. Van Welsesens, C. Borleffs, J. Van Rees, J. Atary, J. Thijssen, E. Van der Wall, M. Schalij, *Neth. Heart J.* **2011**, *19*, 24.
- [21] U. Sigwart, J. J. Goy, L. Finci, M. Blanc, M. Grbic, F. Stumpe, *Clin. Cardiol.* **1986**, *9*, 217.
- [22] N. E. Beurskens, K. T. Breeman, K. J. Dasselaa, A. C. Meijer, A.-F. B. Quast, F. V. Tjong, R. E. Knops, *Expert Rev. Med. Devices* **2019**, *16*, 923.
- [23] H. G. Mond, G. Freitag, *Pacing Clin. Electrophysiol.* **2014**, *37*, 1728.
- [24] C. Ward, S. Henderson, N. H. Metcalfe, *Int. J. Cardiol.* **2013**, *169*, 244.
- [25] K. Jeffrey, V. Parsonnet, *Circulation* **1998**, *97*, 1978.
- [26] V. Parsonnet, A. D. Berstein, G. Y. Perry, *Am. J. Cardiol.* **1990**, *66*, 837.
- [27] V. S. Mallela, V. Iankumaran, N. S. Rao, *Indian Pacing Electrophysiol. J.* **2004**, *4*, 201.
- [28] N. Bhatia, M. El-Chami, *J. Geriatr. Cardiol.* **2018**, *15*, 249.
- [29] M. Kotsakou, I. Kiourmis, G. Lazaridis, G. Pitsiou, S. Lampaki, A. Papaiwannou, A. Karavergou, K. Tsakiridis, N. Katsikogiannis, I. Karapantzos, *Ann. Transl. Med.* **2015**, *3*.
- [30] P. Magnusson, J. V. Pergolizzi, J. A. LeQuang, *Cardiac Pacing and Monitoring: New Methods, Modern Devices*, IntechOpen, London **2018**.
- [31] M. Hosseinipour, R. Gupta, M. Bonnell, M. Elahinia, *J. Rehabil. Assist. Technol. Eng.* **2017**, *4*, 2055668317725994.
- [32] J. H. Karimov, K. Fukamachi, R. C. Starling, *Mechanical Support for Heart Failure: Current Solutions and New Technologies*, Springer Nature, Berlin **2020**.
- [33] J. Al Suwaidi, P. B. Berger, D. R. Holmes Jr, *JAMA, J. Am. Med. Assoc.* **2000**, *284*, 1828.
- [34] D. Katz, T. Akiyama, *Ann. Noninvasive Electrocardiol.* **2007**, *12*, 223.
- [35] A. S. Manolis, T. Maounis, S. Koulouris, V. Vassilikos, *Clin. Cardiol.* **2017**, *40*, 759.
- [36] Z. Taimeh, R. J. Koene, J. Furne, A. Singal, P. M. Eckman, M. D. Levitt, M. R. Pritzker, *J. Heart Lung Transplant.* **2017**, *36*, 625.
- [37] A. Kumar, R. Kiran, V. S. Chauhan, R. Kumar, R. Vaish, *Mater. Res. Express* **2018**, *5*, 075701.
- [38] K. W. Beard, *Linden's Handbook of Batteries*, McGraw-Hill Education, New York **2019**.
- [39] B. H. Waters, J. Park, J. C. Bouwmeester, J. Valdovinos, A. Geirsson, A. P. Sample, J. R. Smith, P. Bonde, *J. Heart Lung Transplant.* **2018**, *37*, 1467.
- [40] A. Aldaoud, J.-M. Redoute, K. Ganesan, G. S. Rind, S. E. John, S. M. Ronayne, N. L. Opie, D. J. Garrett, S. Prawer, *IEEE J. Electromagn., RF Microwaves Med. Biol.* **2018**, *2*, 193.
- [41] J. Drews, G. Fehrmann, R. Staub, R. Wolf, *J. Power Sources* **2001**, *97*, 747.
- [42] R. Ramasamy, C. Feger, T. Strange, B. Popov, *J. Appl. Electrochem.* **2006**, *36*, 487.
- [43] D. C. Bock, A. C. Marschilok, K. J. Takeuchi, E. S. Takeuchi, *J. Power Sources* **2013**, *231*, 219.
- [44] A. Yahiro, S. Lee, D. Kimble, *Biochim. Biophys. Acta, Spec. Sect. Biophys. Subj.* **1964**, *88*, 375.
- [45] K. Rabaey, N. Boon, S. D. Siciliano, M. Verhaege, W. Verstraete, *Appl. Environ. Microbiol.* **2004**, *70*, 5373.
- [46] L. Li, Y. Sun, Z. Yuan, X. Kong, Y. Li, *Environ. Technol.* **2013**, *34*, 1929.
- [47] Y. Han, C. Yu, H. Liu, *Biosens. Bioelectron.* **2010**, *25*, 2156.
- [48] S. D. Minter, B. Y. Liaw, M. J. Cooney, *Curr. Opin. Biotechnol.* **2007**, *18*, 228.
- [49] M. J. Moehlenbrock, S. D. Minter, *Chem. Soc. Rev.* **2008**, *37*, 1188.
- [50] Z. Zhu, T. K. Tam, F. Sun, C. You, Y.-H. P. Zhang, *Nat. Commun.* **2014**, *5*, 3026.
- [51] E. H. Yu, K. Scott, *Energies* **2010**, *3*, 23.
- [52] L. Barelli, G. Bidini, E. Calzoni, A. Cesaretti, A. Di Michele, C. Emiliani, L. Gammaitoni, E. Sisani, in AIP Conf. Proceedings, AIP Publishing, New York **2019**.
- [53] L. Barelli, G. Bidini, D. Pelosi, E. Sisani, *Energies* **2021**, *14*, 910.
- [54] M. Falk, Z. Blum, S. Shleev, *Electrochim. Acta* **2012**, *82*, 191.
- [55] K. MacVittie, J. Halámek, L. Halámková, M. Southcott, W. D. Jemison, R. Lobel, E. Katz, *Energy Environ. Sci.* **2013**, *6*, 81.
- [56] L. Halámková, J. Halámek, V. Bocharova, A. Szczupak, L. Alfonta, E. Katz, *J. Am. Chem. Soc.* **2012**, *134*, 5040.
- [57] A. Szczupak, J. Halámek, L. Halámková, V. Bocharova, L. Alfonta, E. Katz, *Energy Environ. Sci.* **2012**, *5*, 8891.
- [58] J. A. Castorena-Gonzalez, C. Foote, K. MacVittie, J. Halámek, L. Halámková, L. A. Martinez-Lemus, E. Katz, *Electroanalysis* **2013**, *25*, 1579.
- [59] P. Cinquin, C. Gondran, F. Giroud, S. Mazabrard, A. Pellissier, F. Boucher, J.-P. Alcaraz, K. Gorgy, F. Lenouvel, S. Mathé, *PLoS One* **2010**, *5*, e10476.
- [60] T. Miyake, K. Haneda, N. Nagai, Y. Yatagawa, H. Onami, S. Yoshino, T. Abe, M. Nishizawa, *Energy Environ. Sci.* **2011**, *4*, 5008.
- [61] S. El Ichi-Ribault, J.-P. Alcaraz, F. Boucher, B. Boutaud, R. Dalmolin, J. Boutonnat, P. Cinquin, A. Zebda, D. K. Martin, *Electrochim. Acta* **2018**, *269*, 360.
- [62] M. Holzinger, A. Le Goff, S. Cosnier, *Electrochim. Acta* **2012**, *82*, 179.
- [63] M. Lallart, *Small-Scale Energy Harvesting*, IntechOpen, London **2012**.
- [64] N. Sezer, M. Koç, *Nano Energy* **2021**, *80*, 105567.
- [65] G. Shafiq, K. C. Veluvolu, *Sci. Rep.* **2014**, *4*, 5093.
- [66] J. Hlavay, G. Guilbault, *Anal. Chem.* **1977**, *49*, 1890.
- [67] W. Heywang, K. Lubitz, W. Wersing, *Piezoelectricity: Evolution and Future of a Technology*, Vol. 114, Springer Science & Business Media, Berlin **2008**.
- [68] S. Zhang, R. Xia, T. R. Shrout, *J. Electroceram.* **2007**, *19*, 251.
- [69] K. K. Sappati, S. Bhadra, *Sensors* **2018**, *18*, 3605.
- [70] Z. L. Wang, J. Song, *Science* **2006**, *312*, 242.
- [71] B. Lu, Y. Chen, D. Ou, H. Chen, L. Diao, W. Zhang, J. Zheng, W. Ma, L. Sun, X. Feng, *Sci. Rep.* **2015**, *5*, 16065.
- [72] Z. Xu, C. Jin, A. Cabe, D. Escobedo, N. Hao, I. Trase, A. B. Closson, L. Dong, Y. Nie, J. Elliott, *ACS Appl. Mater. Interfaces* **2020**, *12*, 34170.
- [73] S. Azimi, A. Golabchi, A. Nekookar, S. Rabbani, M. H. Amiri, K. Asadi, M. M. Abolhasani, *Nano Energy* **2021**, *83*, 105781.
- [74] S.-E. Park, T. R. Shrout, *J. Appl. Phys.* **1997**, *82*, 1804.
- [75] G. T. Hwang, H. Park, J. H. Lee, S. Oh, K. I. Park, M. Byun, H. Park, G. Ahn, C. K. Jeong, K. No, *Adv. Mater.* **2014**, *26*, 4880.
- [76] C. Covaci, A. Gontean, *Sensors* **2020**, *20*, 3512.
- [77] M. Amin Karami, D. J. Inman, *Appl. Phys. Lett.* **2012**, *100*, 042901.

- [78] M. Ansari, M. A. Karami, *Smart Mater. Struct.* **2017**, *26*, 065001.
- [79] N. Sharpes, A. Abdelkefi, S. Priya, *Appl. Phys. Lett.* **2015**, *107*, 093901.
- [80] X. Li, M. Sun, X. Wei, C. Shan, Q. Chen, *Nanomaterials* **2018**, *8*, 188.
- [81] Z. Lin, J. Chen, J. Yang, *J. Nanomater.* **2016**, *2016*, 5651613.
- [82] J. Chen, Z. L. Wang, *Joule* **2017**, *1*, 480.
- [83] Q. Zheng, B. Shi, Z. Li, Z. L. Wang, *Adv. Sci.* **2017**, *4*, 1700029.
- [84] C. Wu, A. C. Wang, W. Ding, H. Guo, Z. L. Wang, *Adv. Energy Mater.* **2019**, *9*, 1802906.
- [85] Z. L. Wang, J. Chen, L. Lin, *Energy Environ. Sci.* **2015**, *8*, 2250.
- [86] F.-R. Fan, Z.-Q. Tian, Z. L. Wang, *Nano Energy* **2012**, *1*, 328.
- [87] Y. Zhou, W. Deng, J. Xu, J. Chen, *Cell Rep. Phys. Sci.* **2020**, *1*, 100142.
- [88] A. Ahmed, I. Hassan, A. M. Pourrahimi, A. S. Helal, M. F. El-Kady, H. Khassaf, R. B. Kaner, *Adv. Mater. Technol.* **2020**, *5*, 2000520.
- [89] Y. Zou, J. Xu, K. Chen, J. Chen, *Adv. Mater. Technol.* **2021**, *6*, 2000916.
- [90] H. Y. Li, L. Su, S. Y. Kuang, C. F. Pan, G. Zhu, Z. L. Wang, *Adv. Funct. Mater.* **2015**, *25*, 5691.
- [91] Q. Zheng, B. Shi, F. Fan, X. Wang, L. Yan, W. Yuan, S. Wang, H. Liu, Z. Li, Z. L. Wang, *Adv. Mater.* **2014**, *26*, 5851.
- [92] Q. Zheng, H. Zhang, B. Shi, X. Xue, Z. Liu, Y. Jin, Y. Ma, Y. Zou, X. Wang, Z. An, *ACS Nano* **2016**, *10*, 6510.
- [93] Z. Liu, Y. Ma, H. Ouyang, B. Shi, N. Li, D. Jiang, F. Xie, D. Qu, Y. Zou, Y. Huang, *Adv. Funct. Mater.* **2019**, *29*, 1807560.
- [94] H. Ouyang, Z. Liu, N. Li, B. Shi, Y. Zou, F. Xie, Y. Ma, Z. Li, H. Li, Q. Zheng, *Nat. Commun.* **2019**, *10*, 1821.
- [95] A. Chakraborty, B. Saha, S. Koyama, K. C. Ng, *Int. J. Heat Mass Transfer* **2006**, *49*, 3547.
- [96] L. E. Bell, *Science* **2008**, *321*, 1457.
- [97] D. Kraemer, J. Sui, K. McEnaney, H. Zhao, Q. Jie, Z. Ren, G. Chen, *Energy Environ. Sci.* **2015**, *8*, 1299.
- [98] H. Alam, S. Ramakrishna, *Nano Energy* **2013**, *2*, 190.
- [99] L. Yang, Z. G. Chen, M. S. Dargusch, J. Zou, *Adv. Energy Mater.* **2018**, *8*, 1701797.
- [100] C.-J. Yao, H.-L. Zhang, Q. Zhang, *Polymers* **2019**, *11*, 107.
- [101] H. Jin, J. Li, J. Iocozzia, X. Zeng, P. C. Wei, C. Yang, N. Li, Z. Liu, J. H. He, T. Zhu, *Angew. Chem., Int. Ed.* **2019**, *58*, 15206.
- [102] L. Wang, Q. Yao, H. Bi, F. Huang, Q. Wang, L. Chen, *J. Mater. Chem. A* **2015**, *3*, 7086.
- [103] E. J. Bae, Y. H. Kang, K.-S. Jang, S. Y. Cho, *Sci. Rep.* **2016**, *6*, 18805.
- [104] N. Toshima, *Synth. Met.* **2017**, *225*, 3.
- [105] Z.-S. Deng, J. Liu, *Comput. Biol. Med.* **2004**, *34*, 495.
- [106] Y. Yang, X.-J. Wei, J. Liu, *J. Phys. D: Appl. Phys.* **2007**, *40*, 5790.
- [107] D. Bhatia, S. Bairagi, S. Goel, M. Jangssra, *J. Pharm. BioAllied Sci.* **2010**, *2*, 51.
- [108] Y. Yang, G. D. Xu, J. Liu, *J. Med. Devices* **2014**, *8*, 014507.
- [109] M. Yuan, R. Das, E. McGlynn, R. Ghannam, Q. H. Abbasi, H. Heidari, *IEEE Sens. J.* **2021**, *21*, 12484.
- [110] R. Das, F. Moradi, H. Heidari, *IEEE Trans. Biomed. Circuits Syst.* **2020**, *14*, 343.
- [111] E. McGlynn, V. Nabaei, E. Ren, G. Galeote-Checa, R. Das, G. Curia, H. Heidari, *Adv. Sci.* **2021**, *8*, 2002693.
- [112] J. D. Madigan, A. F. Choudhri, J. Chen, H. M. Spotnitz, M. C. Oz, N. Edwards, *Ann. Surg.* **1999**, *230*, 639.
- [113] E. G. Kilinc, M. A. Ghanad, F. Maloberti, C. Dehollain, *IEEE Trans. Biomed. Circuits Syst.* **2014**, *9*, 113.
- [114] K.-L. Wong, *Microwave J.* **2003**, *46*, 144.
- [115] P. Soontornpipit, C. M. Furse, Y. C. Chung, *IEEE Trans. Microwave Theory Tech.* **2004**, *52*, 1944.
- [116] K. Zhang, C. Liu, X. Liu, H. Guo, X. Yang, *Int. J. Antennas Propag.* **2017**, *2017*, 9750257.
- [117] S. Ding, S. Koulouridis, L. Pichon, in 2019 13th European Conf. on Antennas and Propagation (EuCAP), IEEE, Piscataway, NJ **2019**.
- [118] S. Salama, D. Zyoud, R. Daghlal, A. Abuelhaija, *J. Phys.: Conf. Ser.* **2020**, *1711*, 012001.
- [119] M. S. Islam, M. T. Islam, M. A. Ullah, G. K. Beng, N. Amin, N. Misran, *IEEE Access* **2019**, *7*, 127850.
- [120] W. Huang, A. A. Kishk, *Int. J. Antennas Propag.* **2011**, *2011*, 919821.
- [121] A. Ahmad, F. Arshad, S. I. Naqvi, Y. Amin, H. Tenhunon, J. Loo, *IETE J. Res.* **2020**, *66*, 22.
- [122] W. A. Awan, N. Hussain, T. T. Le, *AEU - Int. J. Electron. Commun.* **2019**, *110*, 152851.
- [123] M. Zada, H. Yoo, *IEEE Trans. Antennas Propag.* **2018**, *66*, 7378.
- [124] T. J. Warnagiris, T. J. Minardo, *IEEE Trans. Antennas Propag.* **1998**, *46*, 1797.
- [125] J. Rashed, C.-T. Tai, *IEEE Trans. Antennas Propag.* **1991**, *39*, 1428.
- [126] C. A. Balanis, Microstrip and mobile communications antennas, In *Antenna Theory, Analysis and Design*, Wiley **2016**, pp. 785–787.
- [127] Z. Bendahmane, S. Ferouani, C. Sayah, *Prog. Electromagn. Res.* **2020**, *102*, 163.
- [128] J. H. Kim, C.-H. Ahn, J.-K. Bang, *IEEE Tran. Antennas Propag.* **2016**, *64*, 1164.
- [129] R. Porath, *IEEE Tran. Antennas Propag.* **2000**, *48*, 41.
- [130] R. R. Hasan, M. A. Rahman, S. Sinha, M. N. Uddin, T.-S. R. Niloy, in 2019 Int. Conf. on Automation, Computational and Technology Management (ICACTM), IEEE, Piscataway, NJ **2019**.
- [131] M. Zada, I. A. Shah, A. Basir, H. Yoo, *IEEE Trans. Antennas Propag.* **2020**, *69*, 1152.
- [132] I. A. Shah, M. Zada, H. Yoo, *IEEE Trans. Antennas Propag.* **2019**, *67*, 4230.
- [133] M. Ramzan, X. Fang, Q. Wang, N. Neumann, D. Plettemeier, in 2019 13th Int. Symp. on Medical Information and Communication Technology (ISMICT), IEEE, Piscataway, NJ **2019**.
- [134] Z.-J. Yang, L. Zhu, S. Xiao, *IEEE Trans. Antennas Propag.* **2018**, *66*, 5180.
- [135] X. Chen, B. Assadsangabi, Y. Hsiang, K. Takahata, *Adv. Sci.* **2018**, *5*, 1700560.
- [136] C.-H. Liu, S.-C. Chen, H.-M. Hsiao, *Sensors* **2019**, *19*, 4616.
- [137] T. Nan, H. Lin, Y. Gao, A. Matyushov, G. Yu, H. Chen, N. Sun, S. Wei, Z. Wang, M. Li, *Nat. Commun.* **2017**, *8*, 296.
- [138] E. McGlynn, R. Das, H. Heidari, in 2020 27th IEEE Int. Conf. on Electronics, Circuits and Systems (ICECS), IEEE, Piscataway, NJ **2020**.
- [139] H. Lin, M. Zaeimbashi, N. Sun, X. Liang, H. Chen, C. Dong, A. Matyushov, X. Wang, Y. Guo, Y. Gao, in 2018 IEEE Int. Microwave Biomedical Conf. (IMBioC), IEEE, Piscataway, NJ **2018**.
- [140] M. Zaeimbashi, M. Nasrollahpour, A. Khalifa, A. Romano, X. Liang, H. Chen, N. Sun, A. Matyushov, H. Lin, C. Dong, *Nat. Commun.* **2021**, *12*, 1.
- [141] S. Shevlin, *Nat. Mater.* **2019**, *18*, 191.
- [142] Y. Cheng, B. Peng, Z. Hu, Z. Zhou, M. Liu, *Phys. Lett. A* **2018**, *382*, 3018.
- [143] M. A. Jensen, Y. Rahmat-Samii, *Proc. IEEE* **1995**, *83*, 7.
- [144] Federal Communication Commission, Guidelines for evaluating the environmental effects of radiofrequency radiation, Report and order **1996**.
- [145] IEEE Standards Coordinating Committee, IEEE C95.1-1991, **1992**.
- [146] X. Liu, H.-J. Chen, Y. Alfidhli, X. Chen, C. Parini, D. Wen, *J. Appl. Phys.* **2013**, *113*, 074902.
- [147] D. Miklavčič, N. Pavšelj, F. X. Hart, *Wiley Encycl. Biomed. Eng.* **2006**.
- [148] M. Shahpari, D. V. Thiel, *IEEE Trans. Antennas Propag.* **2015**, *63*, 4686.
- [149] M. Grzeskowiak, F. El Hatmi, A. Diet, M. Benamara, D. Delcroix, T. Alves, S. Protat, S. Mostarshedi, O. Picon, Y. Le Bihan, *C. R. Phys.* **2015**, *16*, 819.
- [150] M. M. Rahman, G. Rather, *J. Sci.: Adv. Mater. Devices* **2020**, *5*, 134.
- [151] K. N. Bocan, M. H. Mickle, E. Sejdici, *IEEE Trans. Microwave Theory Tech.* **2018**, *66*, 3547.

- [152] C.-K. Wu, T.-F. Chien, C.-L. Yang, C.-H. Luo, *Int. J. Antennas Propag.* **2012**, 2012, 564092.
- [153] M. Vallejo, J. Recas, P. G. Del Valle, J. L. Ayala, *Sensors* **2013**, 13, 7546.
- [154] A. A. Y. Ibraheem, M. Manteghi, *Prog. Electromagn. Res.* **2014**, 40, 57.
- [155] M. A. I. Oni, S. H. Shehab, S. R. Khurshid, M. Badruzzaman, S. Dey, *Am. Acad. Scholarly Res. J.* **2015**, 7, 96.
- [156] A. Shon, J.-U. Chu, J. Jung, H. Kim, I. Youn, *Sensors* **2018**, 18, 1.
- [157] K. Chang, *RF and Microwave Wireless Systems*, Vol. 161, John Wiley & Sons, New York **2004**.
- [158] M. Adeeb, A. Islam, M. Haider, F. Tulip, M. Ericson, S. Islam, *Act. Passive Electron. Compon.* **2012**, 2012, 879294.
- [159] A. Kurs, A. Karalis, R. Moffatt, J. D. Joannopoulos, P. Fisher, M. Soljačić, *Science* **2007**, 317, 83.
- [160] J. Kim, H.-C. Son, K.-H. Kim, Y.-J. Park, *IEEE Antennas Wireless Propag. Lett.* **2011**, 10, 389.
- [161] A. P. Sample, D. T. Meyer, J. R. Smith, *IEEE Trans. Ind. Electron.* **2010**, 58, 544.
- [162] V. Vijayakumaran Nair, J. R. Choi, *Energies* **2016**, 9, 156.
- [163] Y. Zhang, Z. Huo, X. Wang, X. Han, W. Wu, B. Wan, H. Wang, J. Zhai, J. Tao, C. Pan, *Nat. Commun.* **2020**, 11, 1.
- [164] D. Ahn, S. Hong, *IEEE Trans. Ind. Electron.* **2013**, 61, 1193.
- [165] S. D. Barman, A. W. Reza, N. Kumar, M. E. Karim, A. B. Munir, *Renewable Sustainable Energy Rev.* **2015**, 51, 1525.
- [166] D. H. Tran, W. Choi, *IEEE Trans. Power Electron.* **2017**, 33, 175.
- [167] Z. Dang, J. A. A. Qahouq, in 2015 IEEE Applied Power Electronics Conf. and Exposition (APEC), IEEE, Piscataway, NJ **2015**.
- [168] G. Monti, P. Arcuti, L. Tarricone, *IEEE Trans. Microwave Theory Tech.* **2015**, 63, 3814.
- [169] P. Yellappa, Y. R. Lee, J. R. Choi, in 2018 IEEE Int. Symp. on Circuits and Systems (ISCAS), IEEE, Piscataway, NJ **2018**.
- [170] R. Huang, B. Zhang, D. Qiu, Y. Zhang, *IEEE Trans. Magn.* **2014**, 50, 1.
- [171] W. Y. Po, S. i. Warisawa, in 2020 IEEE Wireless Power Transfer Conf. (WPTC), IEEE, Piscataway, NJ **2020**.
- [172] R. Jegadeesan, K. Agarwal, Y.-X. Guo, S.-C. Yen, N. V. Thakor, *IEEE Trans. Microwave Theory Tech.* **2016**, 65, 280.
- [173] A. M. Sodagar, P. Amiri, in 2009 4th Int. IEEE/EMBS Conf. on Neural Engineering, IEEE, Piscataway, NJ **2009**.
- [174] R. Erfani, F. Marefat, A. M. Sodagar, P. Mohseni, *IEEE Trans. Circuits Syst., II* **2017**, 65, 923.
- [175] M. Kline, I. Izyumin, B. Boser, S. Sanders, in 2011 Twenty-Sixth Annual IEEE Applied Power Electronics Conf. and Exposition (APEC), IEEE, Piscataway, NJ **2011**.
- [176] H. Zhang, F. Lu, H. Hofmann, W. Liu, C. C. Mi, *IEEE Trans. Power Electron.* **2016**, 31, 8541.
- [177] R. Narayanamoorthi, *IEEE Trans. Compon., Packag., Manuf. Technol.* **2019**, 9, 1253.
- [178] F. Lu, H. Zhang, C. Mi, *Energies* **2017**, 10, 1752.
- [179] K. Keerthi, K. Ilango, G. N. Manjula, in 2018 2nd Int. Conf. on Biomedical Engineering (IBIOMED), IEEE, Piscataway, NJ **2018**.
- [180] J. S. Ho, A. J. Yeh, E. Neofytou, S. Kim, Y. Tanabe, B. Patlolla, R. E. Beygui, A. S. Poon, *Proc. Natl. Acad. Sci. USA* **2014**, 111, 7974.
- [181] A. S. Poon, S. O'Driscoll, T. H. Meng, in 2007 29th Annual Int. Conf. of the IEEE Engineering in Medicine and Biology Society, IEEE, Piscataway, NJ **2007**.
- [182] R. Das, Y. Cho, H. Yoo, in 2016 IEEE MTT-S Int. Microwave Symp. (IMS), IEEE, Piscataway, NJ **2016**.
- [183] A. Basir, H. Yoo, *IEEE Trans. Microwave Theory Tech.* **2020**, 68, 1943.
- [184] N. Nguyen, N. Ha-Van, C. Seo, *IEEE Antennas Wireless Propag. Lett.* **2020**, 19, 2270.
- [185] F. H. Sumi, L. Dutta, F. Sarker, *J. Electr. Electron. Syst.* **2018**, 7, 279.
- [186] X. Lu, P. Wang, D. Niyato, D. I. Kim, Z. Han, *IEEE Commun. Surv. Tutorials* **2015**, 18, 1413.
- [187] R. Gonçalves, N. B. Carvalho, P. Pinho, C. R. Phys. **2017**, 18, 78.
- [188] M. Xia, S. Aissa, *IEEE Trans. Signal Process.* **2015**, 63, 2835.
- [189] J. Huang, Y. Zhou, Z. Ning, H. Gharavi, *IEEE Wireless Commun.* **2019**, 26, 163.
- [190] G. Sun, Y. Liu, H. Li, S. Liang, A. Wang, B. Li, *Int. J. Antennas Propag.* **2018**, 2018, 4867851.
- [191] W. C. Brown, *IEEE Trans. Microwave Theory Tech.* **1984**, 32, 1230.
- [192] H. Sun, Y.-x. Guo, M. He, Z. Zhong, *IEEE Antennas Wireless Propag. Lett.* **2012**, 11, 929.
- [193] C. Liu, Y.-X. Guo, H. Sun, S. Xiao, *IEEE Trans. Antennas Propag.* **2014**, 62, 5798.
- [194] C. Liu, Y. Zhang, X. Liu, *IEEE Antennas Wireless Propag. Lett.* **2018**, 17, 373.
- [195] J. Heikkinen, M. Kivikoski, *IEEE Antennas Wireless Propag. Lett.* **2003**, 2, 330.
- [196] S. M. Asif, A. Iftikhar, J. W. Hansen, M. S. Khan, D. L. Ewert, B. D. Braaten, *IEEE Access* **2018**, 7, 1139.
- [197] A. Abdi, H. Aliakbarian, *IEEE J. Transl. Eng. Health Med.* **2019**, 7, 1900311.
- [198] M. Haerinia, R. Shadid, *Signals* **2020**, 1, 209.
- [199] S. Mandal, R. Sarpeshkar, *IEEE Trans. Biomed. Circuits Syst.* **2008**, 2, 301.
- [200] A. Trigui, M. Ali, S. Hached, J.-P. David, A. C. Ammari, Y. Savaria, M. Sawan, *IEEE Trans. Circuits Syst., I* **2020**, 67, 3978.
- [201] B. Lee, M. Ghovanloo, *IEEE Commun. Mag.* **2019**, 57, 74.
- [202] M. A. Hannan, S. M. Abbas, S. A. Samad, A. Hussain, *Sensors* **2012**, 12, 297.
- [203] G. S. Kishore, H. Rallapalli, in 2019 Int. Conf. on Communication and Signal Processing (ICCSP), IEEE, Piscataway, NJ **2019**.
- [204] A. Trigui, S. Hached, A. C. Ammari, Y. Savaria, M. Sawan, *IEEE Rev. Biomed. Eng.* **2018**, 12, 72.
- [205] M. Ghovanloo, K. Najafi, *IEEE Trans. Circuits Syst., I* **2004**, 51, 2374.
- [206] C. Luo, M. Médard, in *Proceedings of the Annual Allerton Conf. on Communication Control and Computing*, IEEE, Piscataway, NJ **2002**.
- [207] Y. Hu, M. Sawan, *IEEE Trans. Circuits Syst., I* **2005**, 52, 2552.
- [208] J. Jang, H. Cho, H.-J. Yoo, in 2019 IEEE Biomedical Circuits and Systems Conf. (BioCAS), IEEE, Piscataway, NJ **2019**.
- [209] G. Simard, M. Sawan, D. Massicotte, *IEEE Trans. Biomed. Circuits Syst.* **2010**, 4, 192.
- [210] Z.-l. Wei, W.-k. Chen, M.-j. Yang, Y.-M. Gao, Ž. L. Vasić, M. Cifrek, in 2020 IEEE Int. Instrumentation and Measurement Technology Conf. (I2MTC), IEEE, Piscataway, NJ **2020**.
- [211] a) Z. Tang, B. Smith, J. Schild, P. H. Peckham, *IEEE Trans. Biomed. Eng.* **1995**, 42, 524; b) A. Aldaoud, J.-M. Redoute, K. Ganesan, G. S. Rind, S. E. John, S. M. Ronayne, N. L. Opie, D. J. Garrett, S. Praver, *IEEE Sens. Lett.* **2018**, 2, 7501004.
- [212] C. Gong, D. Liu, Z. Miao, W. Wang, M. Li, *Sensors* **2017**, 17, 1358.
- [213] S. Mao, H. Wang, C. Zhu, Z.-H. Mao, M. Sun, *Measurement* **2017**, 109, 316.
- [214] L. Zhou, N. Donaldson, *Neuromodulation* **2003**, 6, 116.
- [215] D. Jiang, D. Cirmirakis, M. Schormans, T. A. Perkins, N. Donaldson, A. Demosthenous, *IEEE Trans. Biomed. Circuits Syst.* **2016**, 11, 64.
- [216] S. Ha, C. Kim, J. Park, S. Joshi, G. Cauwenberghs, *IEEE J. Solid-State Circuits* **2016**, 51, 2664.
- [217] J. S. Ho, S. Kim, A. S. Poon, *Proc. IEEE* **2013**, 101, 1369.
- [218] R. Das, H. Yoo, *IEEE Microwave Wireless Compon. Lett.* **2015**, 25, 262.



Jungang Zhang received her B.Eng. degree in automation from Beijing Institute of Fashion Technology in 2019, CHN, with a focus on the design of wearable fabric electrodes and its front-end adjustment circuit. She received her M.Sc. degree in electronics and electrical engineering from the University of Nottingham, UK, in 2020. She is currently pursuing her Ph.D. as part of the Microelectronics Lab at the University of Glasgow. Her research interest includes wireless power transfer for self-reported implantable medical devices.



Rupam Das received his M.Sc. and Ph.D. degrees in biomedical engineering from the University of Ulsan, Ulsan, South Korea, in 2013 and 2017, respectively. He has been recently awarded the prestigious Marie Curie fellowship to work on wireless neural implants at the University of Glasgow. His current research interests include wireless power transfer, microelectronics, MRI safety, metamaterials, implantable devices, and antennas.



Jinwei Zhao is a bioelectronics engineer in QV Bioelectronics Ltd with expertise in implantable electronic devices. Following on from completing his B.Eng. degree in electrical and electronics engineering at the University of Edinburgh, Jin received a distinction M.Sc. degree in electric power from Newcastle University. He has titled Ph.D. in the University of Glasgow on September 2021. During his Ph.D., Dr. Zhao participated in the Science and Technology Development Fund funded project “High-efficiency Energy Harvesting System for Biomedical Devices” and exchanged to the State Key Laboratory of Analog and Mixed-Signal VLSI group (University of Macau).



Nosrat Mirzai is the former head of the bioelectronics unit and is now affiliated to the College of Medical, Veterinary and Life Sciences, at University of Glasgow, United Kingdom. He managed a team of specialists for 8 years and supervised for 18 years. From 1997 to 2007, he was a deputy manager of the Bioelectronics Unit in the Institute of Biomedical and Life Sciences, focusing on design development of advanced bespoke electronics for Medical/Biomedical and Life Sciences research applications. From 2007 to 2020, he was the head of the Bioelectronics Unit of the College of Medical, Veterinary and Life Sciences, at University of Glasgow, United Kingdom.



John Mercer is a senior lecturer at the Institute of Cardiovascular and Medicine Science at the University of Glasgow. He graduated from Oxford Brookes with a B.Sc. (Hons) in cell and molecular biology in 1995, and then undertook an M.Phil./Ph.D. investigating the emerging role of p53 in radiation induced mutations in thyroid cancer at Berkeley, University of St Andrews, in 2000. For his postdoctoral research, he joined the University of Cambridge, Department of Medicine, at Addenbrooke's hospital. He investigated the inducible role of p53 in vascular smooth muscle cell biology, with a significant emphasis of developing transgenic mouse models of disease.



Hadi Heidari is an associate professor (senior lecturer) in the James Watt School of Engineering at the University of Glasgow, United Kingdom. His Microelectronics Lab (meLAB) conducts pioneering research on integrated microelectronics design and magnetoelectronics device technologies. He holds a Royal Society of Edinburgh Saltire Fellowship. His research has been funded circa £3m by major research councils and funding organizations. He is a senior member of IEEE and a fellow of Higher Education Academy (FHEA). He is a member of the IEEE Sensors Council Member-at-Large (2020–21 and 2022–23) and an associate editor-in-chief of IEEE Journal on Emerging and Selected Topics in Circuits and Systems.